J. Fluid Mech. (1985), *vol.* 159, *pp.* 195–226
Printed in Great Britain

Stokes flow in arbitrary two-dimensional domains: shear flow over ridges and cavities

By JONATHAN J. L. HIGDON

Department of Chemical Engineering, University of Illinois at Urbana-Champaign, 1209 W. California Street, Urbana, Illinois 61821

(Received 7 September 1984 and in revised form 5 April 1985)

A method is described for solving the integral equations governing Stokes flow in arbitrary two-dimensional domains. It is demonstrated that the boundary-integral method provides an accurate, efficient and easy-to-implement strategy for the solution of Stokes-flow problems. Calculations are presented for simple shear flow in a variety of geometries including cylindrical and rectangular, ridges and cavities. A full description of the flow field is presented including streamline patterns, velocity profiles and shear-stress distributions along the solid surfaces. The results are discussed with special relevance to convective transport processes in low-Reynolds-number flows.

1. Introduction

Many problems of physical interest involve the flow of fluids at low Reynolds numbers in two-dimensional geometries. In this paper we describe a procedure for the solution of these problems in arbitrary domains and examine detailed solutions for the specific problem of shear flow over ridges and cavities. A number of studies of Stokes flow in cavities have been motivated by the fundamental interest in the phenomenon of separated flow at low Reynolds numbers. Others have addressed specific problems such as estimating the hole-pressure error when inertial or non-Newtonian effects are included. More generally, a variety of interesting problems are associated with convective-transport processes in low-Reynolds-number flows.

An interesting class of problems involving low-Reynolds-number convection arises when a surface is dissolving or being deposited by mass transfer. In this case, there is a complicated interaction betwen the fluid flow and the convective mass transfer. The fluid flow affects the local-mass-transfer rates and the shape of the evolving surface, which in turn affects the flow pattern. In this way, surfaces of unusual and complex geometries arise. This sequence of events occurs in a number of physical processes. For dissolving boundaries these include natural erosion, as well as corrosion and etching. For surfaces of deposition the convective transport affects the microstructure in the solidification of alloys and the deposition of films by electroplating or chemical plating. These last applications are extremely important in the fabrication of microelectronic components.

Another type of problem for which convection plays an important role is the cleansing of a rough surface that has been exposed to contaminants or toxic compounds. Due to the presence of recirculating eddies in microscopic surface pores, it is very difficult to remove all traces of the undesired element. A precise description of the microscopic flow field can help determine the most effective procedure.

There are a number of other areas in the industrial environment and in natural

systems where low-Reynolds-number flows are important. The industrial applications include the effect of surface roughness on lubrication, the design of polymer dies for favourable extension rates and the development of peristaltic pumps for sensitive viscous materials. In natural systems, low-Reynolds-number flows are important in biomedical applications and studies of animal locomotion.

We have seen that there is a wealth of applications for low-Reynolds-number flows in quite arbitrary geometries. The solution of these problems requires an efficient method which does not depend on special choices of coordinate surfaces or grid spacings. In the present work we will describe a method which is well suited to these requirements. Before proceeding with our discussion we find it helpful to review past efforts in this area to set out the strengths and weaknesses of alternative strategies. Given the number of papers in this area, we will focus on the more limited subject of two-dimensional flows over ridges and cavities.

Among the important analytical solutions in this area, we note the work of Moffat (1964) who showed the existence of an infinite series of recirculating eddies in corners and wedges. These solutions provide an illustration of the phenomenon of separated flow and give the local-flow pattern in a corner independent of the outer flow driving the motion. For the more specific problem of flow over a semi-infinite plane with ridge or depression, Takematsu (1966) considered flow over a rectangular trench of infinite depth, while Kim (1980) studied the complementary problem of flow over a ridge of zero thickness. O'Neill (1977), Davis & O'Neill (1977) and Wakiya (1975, 1978) studied shear flows past planes with cylindrical ridges and cavities. These papers provide valuable examples of flow over cavities for the special geometries considered. They determine the minimum depth for which separation occurs and show that the separation occurs not at the sharp edge of the cavity, but at a finite distance along the cavity wall. Overall, these analytical solutions illustrate many of the basic features common to all cavity flows. For detailed studies of more general geometries, including finite rectangular cavities, we must turn to numerical calculations.

A variety of numerical techniques have been used to study low-Reynolds-number flows, including finite differences, finite elements, eigenfunction expansions and integral equations. A comprehensive review of the many computations which have been made is given in the review article by Hasimoto & Sano (1980). In the present context we mention certain references which are characteristic of the different numerical methods. Pan & Acrivos (1967) used finite differences to study low-Reynolds-number flows in cavities driven by uniform translation of the top wall. O'Brien (1982, 1983) has also used finite differences to study a variety of Stokes-flow problems involving cavities. Finite-element calculations for similar geometries include those by Malkus (1976) and Jackson & Finlayson (1982). Trogdon & Joseph (1982) and Sanders, O'Brien & Joseph (1980) used eigenfunction expansions for flow over cavities. In the latter paper these were compared with finite-difference calculations and were found to be in good agreement. In the calculations cited above both Newtonian and non-Newtonian fluids have been considered.

We see that a variety of methods have been used for Stokes flow in two-dimensional domains. Each of these methods has its strengths, but all have certain limitations when dealing with irregular geometries and infinite or semi-infinite domains. The finite-difference method and the eigenfunction expansions are most useful for regular geometries or rectangular boundaries. These methods can be adapted to more complex geometries, but become increasingly awkward to use. The finite-element method may be used in arbitrary geometries, but large numbers of elements are required to resolve fine surface detail. As the complexity increases computations

become quite expensive, and the selection of the two-dimensional grid becomes increasingly tedious.

One method which is both efficient and easy to implement in arbitrary geometries is based on the reformulation of the Stokes equations in terms of an integral equation. In this method only the boundary of the domain is discretized, with the result that complicated boundaries can easily be represented and the number of unknowns increases only linearly with increasing resolution. The use of integral equations has been quite common in three-dimensional Stokes-flow problems. Youngren & Acrivos (1975) presented calculations for exterior flows past particles of arbitrary shape; Rallison & Acrivos (1978) studied axisymmetric flow past deformable drops and Lee & Leal (1982) considered the motion of rigid spheres near deformable interfaces. Higdon (1979*a*, *b*) used integral equations based on slender-body theory to study the motion of microscopic organisms. Given this widespread use for three-dimensional calculations, it is surprising that the integral equations have not been used extensively in two dimensions. There are perhaps two reasons for this. The first is that the simple problem of uniform flow past a two-dimensional body is a singular-perturbation problem for which the Stokes equations are not uniformly valid. Thus these problems have received less attention overall. Associated with this first reason is the fact that the fundamental solution or Stokeslet for two-dimensions is less well known because it too is singular at infinity. The second reason may be that the more traditional methods discussed above are feasible for two-dimensional calculations but much too expensive for three-dimensions.

In the present effort we employ the integral equations (sometimes referred to as the boundary-integral method) for the solution of Stokes equations in arbitrary two-dimensional domains. In choosing this direction we have two alternatives: to work with the fundamental solution of the Stokes' equations in direct analogy to the three-dimensional calculations or to use the formulation in terms of the stream function and the biharmonic equation. Both methods lead to a Fredholm equation which is converted into a system of linear algebraic equations. In the biharmonic approach it can be shown that an iterative solution will converge for all geometries (Mikhlin 1957, p. 219) thus eliminating the need for a matrix inversion. In practice this is not a major advantage, since the calculation of the matrix elements requires the most computational effort for systems of up to 200 boundary elements.

Mir-Mohamad-Sadegh & Rajagopal (1980) have used the biharmonic approach for flow over cavities, but have given only limited results with crude qualitative sketches of the streamlines. We prefer to work directly with the Stokes equations. The computational effort is the same in either case, but the use of the Stokes equations leads to the direct calculation of the surface force and velocity, rather than the fictitious source densities resulting from the biharmonic approach. We shall show that this method combines the features of ease of use, excellent accuracy and great computational efficiency. It would appear to be the best choice for Stokes flow in complicated domains.

In summary we have two objectives. The first is to present a clear description of the boundary-integral method, including an explanation of its numerical implementation and a demonstration of its efficiency. The second is to use the method to examine shear flows over ridges and cavities, giving detailed streamline patterns and distributions of shear stress over the boundaries. These results are employed in a discussion of the effect of the flow pattern on convective transport processes.

2. Mathematical formulation

In this section we transform the Stokes equations with boundary conditions into an equivalent set of integral equations. The simplest approach would be to cite the relevant results for three-dimensional flows and make the appropriate substitutions required for two-dimensions. We prefer to give a more detailed discussion, believing that many researchers may not be familiar with the exact assumptions and analysis involved.

The basic equations governing flow at low Reynolds number are the Stokes equations

$$\nabla\cdot\boldsymbol{\sigma} \equiv -\nabla p+\mu\nabla^2\boldsymbol{u} = 0, \tag{1}$$

and the continuity equation

$$\nabla\cdot\boldsymbol{u} = 0. \tag{2}$$

In the above equations $\boldsymbol{\sigma}$, the stress tensor for a Newtonian fluid, is defined in the standard form:

$$\sigma_{ij} = -p\delta_{ij}+\mu\left(\frac{\partial u_i}{\partial x_j}+\frac{\partial u_j}{\partial x_i}\right). \tag{3}$$

A fundamental identity for Stokes equations, analogous to Green's identity, may be written

$$\frac{\partial}{\partial x_j}(u_i\sigma^*_{ij}-u^*_i\sigma_{ij}) = 0. \tag{4}$$

In this expression, $\boldsymbol{u}$ and $\boldsymbol{u}^*$ are any two solutions of (1) and (2) with associated stress tensors $\boldsymbol{\sigma}$ and $\boldsymbol{\sigma}^*$. This identity is easily verified by direct differentiation and application of (1)–(3). When the identity is integrated over any volume of fluid, the divergence theorem may be applied to yield an integral formula known as the reciprocal theorem

$$\int_S (u_i\sigma^*_{ij}n_j-u^*_i\sigma_{ij}n_j)\,\mathrm{d}S = 0, \tag{5}$$

Lorentz (1896).

When the reciprocal theorem is applied with appropriate choices for the reference solutions $\boldsymbol{u}^*$, $\boldsymbol{\sigma}^*$ many useful results may be obtained (see e.g. Happel & Brenner 1973, chap. 5 and Hinch 1972). To obtain an integral formula suitable for our present purposes, we choose $\boldsymbol{u}^*$ to be the fundamental solution for two-dimensional Stokes flow. Following a procedure introduced by Oseen (see Happel & Brenner 1973, pp. 79–81), we define

$$S_{ij}(\hat{\boldsymbol{x}}) = \delta_{ij}\ln r-\frac{\hat{x}_i\hat{x}_j}{r^2}, \tag{6}$$

where $\hat{\boldsymbol{x}} = \boldsymbol{x}-\boldsymbol{x}_0$ and $r = |\hat{\boldsymbol{x}}|$. The fluid velocity is then given by

$$u_i(\boldsymbol{x}) = S_{ij}(\hat{\boldsymbol{x}})\frac{f_j(\boldsymbol{x}_0)}{4\pi\mu}. \tag{7}$$

Physically, this may be interpreted as the velocity at $\boldsymbol{x}$ induced by a two-dimensional point force $\boldsymbol{f}$ at the point $\boldsymbol{x}_0$. The singular nature of $\boldsymbol{u}$ at infinity is consistent with the non-uniformity of the Stokes equations when there is a net force on a two-dimensional body. This singular behaviour is unimportant in the present circumstances because we shall be concerned with problems for which the Stokes equations are uniformly valid.

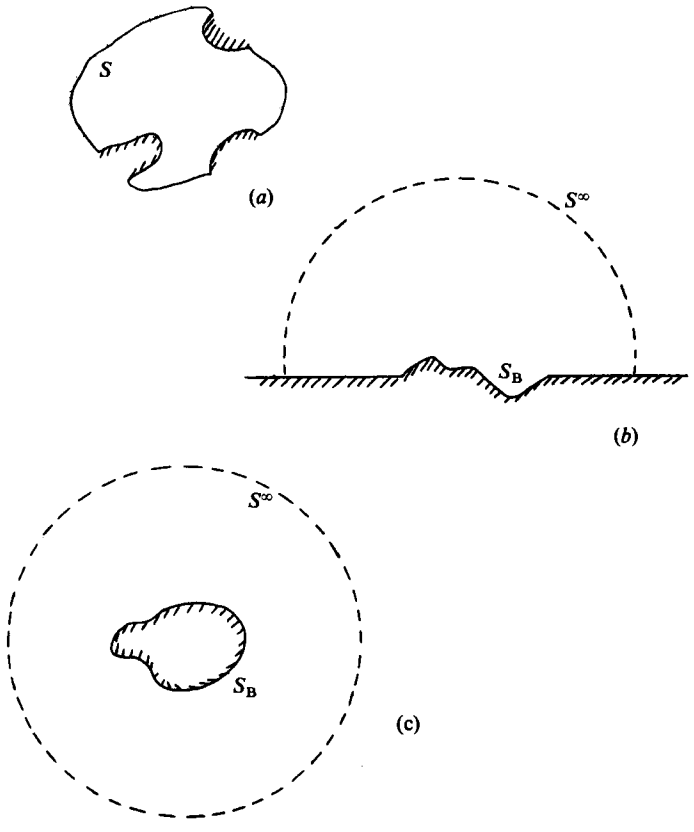

FIGURE 1. Sketch showing boundary surfaces for integral equations. (*a*) interior flows, (*b*) semi-infinite flows, (*c*) exterior flows.

The stress associated with the velocity (7) is given by

$$\sigma_{ik}(\boldsymbol{x}) = T_{ijk}(\hat{\boldsymbol{x}})\frac{f_j(\boldsymbol{x}_0)}{4\pi\mu}, \tag{8}$$

where T_{ijk} is defined as

$$T_{ijk}(\hat{\boldsymbol{x}}) = 4\mu\frac{\hat{x}_i\hat{x}_j\hat{x}_k}{r^4}. \tag{9}$$

Similarly, the pressure is obtained in the form

$$p(\boldsymbol{x}) = -2\mu\frac{\hat{x}_j}{r^2}\frac{f_j(\boldsymbol{x}_0)}{4\pi\mu}. \tag{10}$$

When the integral formula (5) is applied with $\boldsymbol{u}^*$ and $\boldsymbol{\sigma}^*$ given by (7), (8), the boundary surface includes two components: S which represents all surfaces bounding the fluid domain and S_ϵ which is a circle or semi-circle excluding the point $\boldsymbol{x} = \boldsymbol{x}_0$ (see figure 1).

Evaluating the integral over S_ϵ in the limit as $\epsilon \to 0$ yields

$$u_i(\boldsymbol{x}_0) = \frac{1}{4\pi\mu}\int_S (S_{ij}(\hat{\boldsymbol{x}})f_j(\boldsymbol{x}) - T_{ijk}(\hat{\boldsymbol{x}})\,u_j(\boldsymbol{x})\,n_k)\,\mathrm{d}S \tag{11}$$

when the point $\boldsymbol{x}_0$ is in the fluid domain, and

$$u_i(\boldsymbol{x}_0) = \frac{1}{2\pi\mu}\int_S (S_{ij}(\hat{\boldsymbol{x}})f_j(\boldsymbol{x}) - T_{ijk}(\hat{\boldsymbol{x}})\,u_j(\boldsymbol{x})\,n_k)\,\mathrm{d}S \tag{12}$$

when $\boldsymbol{x}_0$ is on the boundary of the domain.

In (11) and (12), $f_j(\boldsymbol{x})$ is the surface-force vector defined as $f_j(\boldsymbol{x}) = \sigma_{jk}(\boldsymbol{x})\,n_k$. The surface integral (which in two-dimensions is merely a line integral) is taken counterclockwise around the outer boundary and the unit normal vector $\boldsymbol{n}$ points out of the fluid.

The integral formula (12) combined with the boundary conditions for the flow yields an integral equation for the unknown quantities $\boldsymbol{u}$ or $\boldsymbol{f}$ around the boundary S. The exact form of the integral equation depends on the boundary conditions and the type of domain. We mention briefly the appropriate forms for interior flows, semi-infinite domains and exterior flows.

For interior-flow problems, figure 1 (*a*), S may consist of fluid surfaces and solid surfaces surrounding the domain. The velocity $\boldsymbol{u}$ and surface force $\boldsymbol{f}$ or some combination of these is specified on all boundaries, and the integral formula may be used in its standard form (12).

For semi-infinite problems, figure 1 (*b*), we typically specify the flow at infinity, e.g. simple shear flow, and require $\boldsymbol{u} = 0$ on the solid boundary. In this case, the boundary S includes the semi-circle S^∞ in addition to the solid surfaces S_B. It is inconvenient to use (12) directly, because of the integral over S^∞, so we define the disturbance velocity $\boldsymbol{u}^\mathrm{D} = \boldsymbol{u} - \boldsymbol{u}^\infty$. Applying (12) with $\boldsymbol{u}^\mathrm{D}$ in place of $\boldsymbol{u}$, the integral over S^∞ may be shown to vanish, and we have

$$u_i^\mathrm{D}(\boldsymbol{x}_0) = \frac{1}{2\pi\mu}\int_{S_\mathrm{B}} (S_{ij}(\hat{\boldsymbol{x}})f_j^\mathrm{D}(\boldsymbol{x}) - T_{ijk}(\hat{\boldsymbol{x}})\,u_j^\mathrm{D}(\boldsymbol{x})\,n_k)\,\mathrm{d}S. \tag{13}$$

The domain of integration has been reduced to the solid surfaces. The integral equation results from the boundary condition $\boldsymbol{u}^\mathrm{D} = -\boldsymbol{u}^\infty$ on the solid surfaces.

For exterior-flow problems, figure 1 (*c*), we again define $\boldsymbol{u}^\mathrm{D}$ and can show that the integral over S^∞ vanishes provided that the total force on the body is zero, i.e.

$$\int_{S_\mathrm{B}} \boldsymbol{f}\,\mathrm{d}S = 0.\dagger$$

Thus (13) is the appropriate integral formula for exterior flows with S_B designating all interior boundary surfaces.

For exterior-flow problems in which all boundary surfaces are rigid and fixed with respect to each other, we may make one additional simplification. The integrals (12) with $\boldsymbol{u}^\infty$ in place of $\boldsymbol{u}$ may be evaluated by applying the divergence theorem over the volume bounded by the interior boundaries. This result may be combined with the boundary condition $\boldsymbol{u}^\mathrm{D} = -\boldsymbol{u}^\infty$ to reduce (13) to the form

$$u_i^\mathrm{D}(\boldsymbol{x}_0) - u_i^\infty(\boldsymbol{x}_0) = \frac{1}{2\pi\mu}\int_{S_\mathrm{B}} S_{ij}(\hat{\boldsymbol{x}})f_j(\boldsymbol{x})\,\mathrm{d}S. \tag{14}$$

We have given the appropriate form of the integral equations for the typical boundary-value problems which arise in two-dimensional Stokes flow. One further

† If the total force on the object is not zero, then the Stokes equations are not uniformly valid and the outer boundary condition must be obtained by matching an outer expansion based on the Navier–Stokes equations.

point needs to be mentioned. For interior- or exterior-flow problems, the solution of (12) or (14) is not unique because an arbitrary constant may be added to the normal component of $\boldsymbol{f}$ without changing the value of the integrals. This is merely a reflection of the fact that a constant pressure may be added without affecting the dynamics of the system. The non-uniqueness may be eliminated by specifying a reference value for the pressure at any point on the boundary. This additional condition does not overconstrain the problem because all velocities defined by the integral formulas above automatically satisfy the integral mass balance

$$\int \boldsymbol{u}\cdot\boldsymbol{n}\,\mathrm{d}S = 0.$$

Thus the additional constraint on p is allowed because the specified boundary values of $\boldsymbol{u}$ are not independent. Finally, we note that this problem does not arise for semi-infinite domains, because it is implicitly assumed that the average value of p over S^{∞} is zero.

3. Numerical procedure

The integral equations derived in the previous section provide a compact and elegant formulation of the boundary-value problem for the Stokes equations. Unfortunately, with the exception of a few special cases, we must resort to numerical methods for the solution of these equations. To obtain a numerical solution the continuous smooth boundary surface is replaced by a number of discrete boundary elements and the boundary values of $\boldsymbol{u}$ and $\boldsymbol{f}$ are expressed in terms of their values at discrete boundary points $\boldsymbol{x}_m$. With these specifications, (12) may be written in the discrete form

$$u_i(\boldsymbol{x}_m) = \sum_{n=1}^{N} A_{ij}(\boldsymbol{x}_m, \boldsymbol{x}_n) f_j(\boldsymbol{x}_n) + \sum_{n=1}^{N} B_{ij}(\boldsymbol{x}_m, \boldsymbol{x}_n)\, u_j(\boldsymbol{x}_n). \tag{15}$$

In this expression, the exact form of A_{ij} and B_{ij} will be determined by the specific discretization which is used. Equation (15) combined with the discretized boundary conditions, e.g. $\boldsymbol{u}$ specified at $\boldsymbol{x}_m$, leads to a system of linear algebraic equations for the unknown values, e.g. $\boldsymbol{f}(\boldsymbol{x}_m)$. This system may be solved using standard algorithms.

We now turn our attention to the choices of discretizations for the boundary and functions, and the errors associated with these choices. For the boundary elements we might choose among straight-line segments, arcs, parabolas, splines or other curves. We find it most convenient to employ straight-line segments because this allows the analytical evaluation of the integrals along each segment. If analytical integrations were not used, the singularities in S_{ij} and T_{ijk} would have to be dealt with before applying any numerical quadratures. For smooth boundaries the deviation of the discrete segments from the true boundary shape is of order $\delta^2\kappa$, where δ is the segment length and κ is the local curvature. Upon evaluating the integrals in (12), we find a relative error of order $\delta^2\kappa^2$. Given this quadratic error term, good accuracy may be obtained with a reasonable number of segments, and the use of more complicated boundary elements is unwarranted. Any gain in accuracy would be offset by the additional effort required for the numerical evaluation of the integrals. For piecewise smooth boundaries, such as a rectangle or the intersection of an arc with a plane, elements are chosen such that the corner lies at the end of a line segment. With this procedure, piecewise smooth boundaries may be treated with the accuracy stated above.

For the approximation of the functions $\boldsymbol{u}$ and $\boldsymbol{f}$ on the boundary we use simple polynomial expressions based on Lagrangian interpolation formulas. For an nth-order polynomial, the relative error in evaluating the integrals in (12) is of order δ^{n+1} or more specifically $\delta^{n+1}f^{(n+1)}/f$. For the calculations in the present paper, we have used two different approximations: constant function values along each segment with an error δ and quadratic polynomials with an error δ^3. In each of these cases the leading-order error in f is an odd function about the centre of the segment. For regions where the boundary is locally symmetric about the segment, the total integrand is odd and these integrals vanish. Thus the relative errors are of order δ^2 and δ^4 respectively.

When constant function values are assumed along each segment, the explicit expressions for A_{ij} and B_{ij} are

$$A_{ij}(\boldsymbol{x}_m, \boldsymbol{x}_n) = \frac{1}{2\pi\mu}\int_{-\delta_n}^{\delta_n} S_{ij}(\boldsymbol{x}_m - \boldsymbol{x}_n - \xi \boldsymbol{t}_n)\,\mathrm{d}\xi, \tag{16}$$

and

$$B_{ij}(\boldsymbol{x}_m, \boldsymbol{x}_n) = \frac{-1}{2\pi\mu}\int_{-\delta_n}^{\delta_n} T_{ijk}(\boldsymbol{x}_m - \boldsymbol{x}_n - \xi \boldsymbol{t}_n)\, n_k\,\mathrm{d}\xi. \tag{17}$$

In these integrals, $\boldsymbol{t}$ and $\boldsymbol{n}$ are the unit vectors tangent and normal to the nth segment, $2\delta_n$ is the length and ξ is the local parametric variable along the segment.

In the case of quadratic approximation a three-point Lagrangian interpolation is used, based on the function values at the centre of the segments. The value of the function $\boldsymbol{f}$ along the nth segment is given by

$$f(\xi) = f_{n-1}(W_n^{\mathrm{L}}\xi + Q_n^{\mathrm{L}}\xi^2) + f_n(1 + W_n^0\xi + Q_n^0\xi^2) + f_{n+1}(W_n^{\mathrm{R}}\xi + Q_n^{\mathrm{R}}\xi^2). \tag{18}$$

The weights W_n, Q_n are simple algebraic functions of δ_{n-1}, δ_n and δ_{n+1} (see Carnahan, Luther & Wilkes 1969, p. 27).

Having approximated the function $\boldsymbol{f}$ over each segment, we may now evaluate its integral and write

$$\begin{aligned}\int_{-\delta_n}^{\delta_n} S_{ij}(\hat{\boldsymbol{x}}) f_j(\boldsymbol{x})\,\mathrm{d}S = {} & (f_{n-1})_j \int_{-\delta_n}^{\delta_n} (W_n^{\mathrm{L}}\xi + Q_n^{\mathrm{L}}\xi^2)\, S_{ij}(\boldsymbol{x}_m - \boldsymbol{x}_n - \xi\boldsymbol{t}_n)\,\mathrm{d}\xi \\ & + (f_n)_j \int_{-\delta_n}^{\delta_n} (1 + W_n^0\xi + Q_n^0\xi^2)\, S_{ij}(\boldsymbol{x}_m - \boldsymbol{x}_n - \xi\boldsymbol{t}_n)\,\mathrm{d}\xi \\ & + (f_{n+1})_j \int_{-\delta_n}^{\delta_n} (W_n^{\mathrm{R}}\xi + Q_n^{\mathrm{R}}\xi^2)\, S_{ij}(\boldsymbol{x}_m - \boldsymbol{x}_n - \xi\boldsymbol{t}_n)\,\mathrm{d}\xi. \end{aligned} \tag{19}$$

We observe that the integral involves values of $\boldsymbol{f}$ from neighbouring segments. To find A_{ij}, we collect terms involving $\boldsymbol{f}_n$ from the nth segment as well as adjacent segments and obtain

$$\begin{aligned} A_{ij}(\boldsymbol{x}_m, \boldsymbol{x}_n) = {} & \frac{1}{2\pi\mu}\int_{-\delta_{n-1}}^{\delta_{n-1}} (W_{n-1}^{\mathrm{R}}\xi + Q_{n-1}^{\mathrm{R}}\xi^2)\, S_{ij}(\boldsymbol{x}_m - \boldsymbol{x}_{n-1} - \xi\boldsymbol{t}_{n-1})\,\mathrm{d}\xi \\ & + \frac{1}{2\pi\mu}\int_{-\delta_n}^{\delta_n} (1 + W_n^0\xi + Q_n^0\xi^2)\, S_{ij}(\boldsymbol{x}_m - \boldsymbol{x}_n - \xi\boldsymbol{t}_n)\,\mathrm{d}\xi \\ & + \frac{1}{2\pi\mu}\int_{-\delta_{n+1}}^{\delta_{n+1}} (W_{n+1}^{\mathrm{L}}\xi + Q_{n+1}^{\mathrm{L}}\xi^2)\, S_{ij}(\boldsymbol{x}_m - \boldsymbol{x}_{n+1} - \xi\boldsymbol{t}_{n+1})\,\mathrm{d}\xi. \end{aligned} \tag{20}$$

The expression for B_{ij} may be found by substituting $-T_{ijk}\,n_k$ for S_{ij}.

The error estimates given above for the function approximation must be modified for the case of a corner on a piecewise smooth boundary. The problem arises in the evaluation of the integral of $T_{ijk}\,n_k$. When the integral is evaluated for $\boldsymbol{x}_m$ adjacent to the nth segment, the term $x_k\,n_k$ is order $\delta^2\kappa$ for a smooth boundary, but only order δ for a corner. The resulting error is thus one order greater. This is no problem for the quadratic representation but can lead to an error of $O(1)$ in the immediate vicinity of the corner if constant function values are assumed. Specifically, the value of B_{ij} will have an $O(1)$ error proportional to $\nabla \boldsymbol{u}$. It should be noted that, even in the worst case, the $O(1)$ error occurs only on the segments adjoining the corner and has negligible effect on the solution away from this point.

We have seen how the continuous integral equation is converted into a set of linear algebraic equations. In our calculations these equations were solved using Gaussian elimination with maximum row pivoting. The residuals were completely negligible for all systems considered, including matrices up to 250×250. The solution of the system of equations provided the values of $\boldsymbol{f}$ on the boundary; velocities in the interior of the domain were calculated using (11) with the integrals evaluated through the procedure described above. Streamlines were drawn by choosing appropriate starting points, calculating the velocity and integrating the ordinary differential equation $\mathrm{d}x/u = \mathrm{d}y/v$. The modified Euler method was used for the numerical integration of the ordinary differential equation with the step size chosen to provide a smooth appearance for the streamline. With this constraint on the step size the modified Euler method gave excellent accuracy, and higher-order methods were not justified.

In the following sections we present the results of calculations for a variety of different geometries. Before proceeding with this discussion, we would like to analyse the numerical results for a number of special cases which confirm our error predictions and illustrate the accuracy of the boundary-integral method. First, we calculated the solution for a circular domain with a transverse velocity $u = y^2$. This is representative of a driven cavity with smooth boundaries. The errors for both the constant and the quadratic approximations decreased uniformly as δ^2, the limiting error in this case being proportional to $\kappa^2\delta^2$. Numerically, the quadratic errors were consistently $\frac{1}{3}$ the constant errors. Next, we considered a square domain with velocity $u = y^2$, characteristic of a driven cavity with corners. In this case the quadratic method should give an exact solution. The relative errors were consistent with this prediction, being of order 10^{-13}, which is the limit associated with round-off error in the computer. For the constant approximation, there was a persistent error of 20 % on the corner segments, independent of δ. The persistent error decreased to 2 % on the next segments and errors decreased as δ^2 on all other segments. This is consistent with predictions.

Next, we turn to problems involving semi-infinite domains. For shear flow over a circular crest, the streamlines are shown in figure 14 (*b*) while the shear stress is plotted in figure 15 (*b*). The errors in shear stress associated with the constant and quadratic approximations are given in table 1. The exact values listed are calculated from the solution of O'Neill (1977). For the constant forces there is a persistent error of 15 % on the corner segments while the errors decrease as δ^2 over the remaining segments. The quadratic method gives an error $O(\delta)$ on the corner segments because no finite number of segments can resolve the infinite sequence of corner eddies using a simple polynomial approximation. On all other segments the errors decrease as δ^2 and are roughly half the size of the constant-method errors.

The streamlines for flow over a circular cavity are shown in figure 3 (*b*) while the shear stress is plotted in figure 5 (*b*). The exact values of the shear stress and numerical

Position: θ/π		0.003125	0.00625	0.0125	0.025	0.050	0.100	0.200	0.300	0.400	0.500
Exact stress		0.00036	−0.00030	−0.00545	−0.02267	−0.04687	0.03683	0.74010	1.80159	2.71034	3.06390
Constant force											
n/N	CPU										
11/45	0.18 s	—	—	—	0.15100	—	0.04916	0.00110	−0.03198	−0.06063	−0.07170
21/67	0.40 s	—	—	0.15540	—	0.03925	0.01195	0.00131	−0. 00807	−0.01560	−0.01849
41/111	1.28 s	—	0.15705	—	0.03889	0.01212	0.00394	0.00038	−0.00214	−0.00411	−0.00486
81/193	5.04 s	0.15809	—	0.04022	0.01314	0.00400	0.00112	0.00003	−0.00070	−0.00125	−0.00145
Quadratic force											
n/N	CPU										
11/45	0.29 s	—	—	—	−0.01865	—	0.00146	0.00009	−0.01910	−0.03507	−0.04133
21/67	0.63 s	—	—	−0.00991	—	0.00114	0.00228	−0.00021	−0.00503	−0.00918	−0.01079
41/111	1.93 s	—	−0.00517	—	−0.00106	0.00031	0.00063	−0.00006	−0.00127	−0.00233	−0.00274
81/193	7.07 s	−0.00255	—	−0.00060	0.00002	0.00012	0.00016	−0.00001	−0.00032	−0.00059	−0.00070

TABLE 1. Comparison of exact shear stress with two numerical methods for shear flow over semicircular crest. Top of crest is $\theta = \frac{1}{2}\pi$, intersection with plane is $\theta = 0$. Numbers n/N are the number of segments on the crest and the total number of segments including the plane boundary. CPU times are for CYBER 175.

Position: θ/π		0.003125	0.00625	0.0125	0.025	0.050	0.100	0.200	0.300	0.400	0.500
Exact stress		0.65463	0.29348	0.05909	−0.07761	−0.13905	−0.14638	−0.12362	−0.10726	−0.09857	−0.09587
Constant force											
n/N	CPU										
11/31	0.09 s	—	—	—	0.43049	—	0.04289	0.00594	−0.01286	−0.02897	−0.03498
21/43	0.17 s	—	—	0.55551	—	0.03815	0.01490	0.00473	−0.00178	−0.00624	−0.00787
41/65	0.42 s	—	0.74081	—	0.04197	0.01754	0.00739	0.00237	0.00026	0.00103	−0.00149
81/107	1.29 s	1.00081	—	0.04740	0.02155	0.00905	0.00345	0.00123	0.00045	0.00003	−0.00011
Quadratic force											
n/N	CPU										
11/31	0.23 s	—	—	—	0.04955	—	−0.01465	0.00927	0.00307	0.00510	0.00556
21/43	0.38 s	—	—	0.05509	—	−0.00751	0.00880	0.00080	0.00084	0.00124	0.00141
41/65	0.82 s	—	0.06122	—	−0.00518	0.00970	0.00074	0.00011	0.00020	0.00032	0.00036
81/107	2.20 s	0.06616	—	−0.00609	0.01124	0.00090	0.00005	0.00000	0.00005	0.00008	0.00010

TABLE 2. Comparison of exact shear stress with two numerical methods for shear flow over semicircular cavity. Bottom of cavity is $\theta = \frac{1}{2}\pi$, intersection with plane is $\theta = 0$. Numbers n/N are the number of segments in the cavity and the total number of segments including the plane boundary. CPU times are for CYBER 175.

errors are given in table 2. In this problem the shear stress has an algebraic singularity ($x^{-0.455\,516}$) at the corners $\theta = 0$. In the constant-force approximation this leads to large errors on the corner segment, as might be expected. The error at the base of the cavity decreases as δ^2, but along the wall (e.g. $\theta/\pi = 0.100$) the error decreases only as δ. Because of the singularity the quadratic-force method offers little improvement over the constant-force method for this problem. Instead, we assume a singular force on the corner segment in the form stated above and use quadratic forces over all other segments. The integrals for the corners could not be evaluated analytically and were calculated using Gaussian quadratures after extracting algebraic and logarithmic singularities. The results of these calculations are listed in table 2. The relative error now decreases as δ^2 over the entire boundary including the corner segments. Note that the error trend at certain positions (e.g. $\theta/\pi = 0.200$) may appear better than δ^2, but this is fortuitous.

In summary, we see that the boundary-integral method is capable of excellent accuracy even in problems involving singular force distributions. The constant-force method will be adequate for nearly all purposes except where extreme accuracy is required at all positions. For such problems the quadratic method or other variations will provide the necessary precision. It should be emphasized that the constant segment length used in tables 1 and 2 was chosen to show the error trend as a function of N. It is *not* the optimal distribution and significant improvements can be made by using progressively smaller segments in corners or regions where the curvature is large or where $\boldsymbol{f}$ changes rapidly.

4. Shear flow over circular cavities

We start our discussion of shear flows in semi-infinite domains by considering circular cavities in a uniform plane. Figure 2 shows the basic geometry and defines the geometrical parameters. This problem has been studied previously by O'Neill (1977) and Wakiya (1975, 1978), both of whom used bipolar cordinates to obtain analytical solutions. We choose to study this geometry for two reasons. First, as noted in the last section, it provides a check on the accuracy of our calculations. Second and more importantly, we note that the analytical solutions which have been obtained are in a rather inconvenient form. Thus neither of the authors above provided detailed streamline patterns nor distributions of shear stress over the boundaries. In the present study we provide this detailed information, which helps to illustrate more clearly the flow over circular cavities.

The first cavity we consider is for angle $\alpha = 65.12°$, corresponding to the deepest cavity for which the flow does not separate from the boundary wall. The streamlines for this flow are shown in figure 3(*a*). In this figure, and in all streamline plots shown, the streamlines outside the cavity are drawn with equal spacing far upstream. Streamlines within a separated cavity are spaced for maximum clarity. This choice was made to present the best view of the overall flow pattern. For shear flows such as studied in this paper, the conventional method of drawing streamlines with constant volume flux leads to an unfortunate spacing which obscures important details of the motion. All streamlines shown are accurate to within a plotted line width.

The streamlines in figure 3(*a*) show that the cavity has a rather weak effect on the major part of the flow but results in strong deceleration of the fluid adjacent to the boundary. A clearer view of the flow is given by examining the velocity profile along the symmetry axis of the cavity, as shown in figure 4(*a*). The vertical intercept at

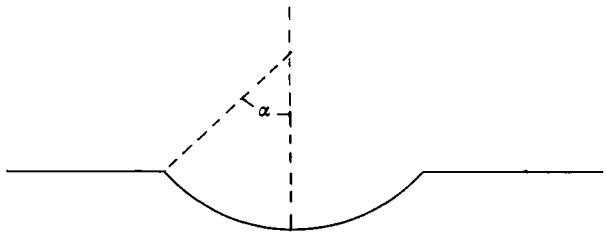

FIGURE 2. Sketch showing geometry for circular cavities.

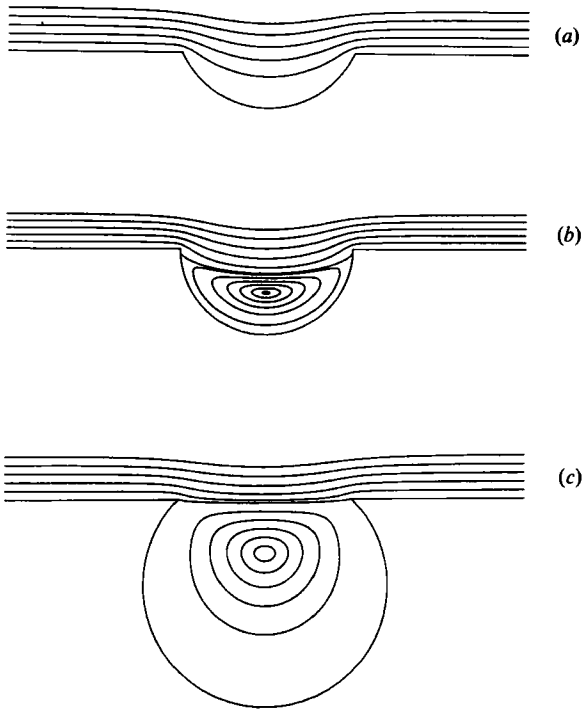

FIGURE 3. Streamline patterns for simple shear flow over circular cavities. Undisturbed flow is $u = \dot{\gamma}y$, $v = 0$. (*a*) $\alpha = 65.12°$, (*b*) 90°, (*c*) 135°.

the bottom implies $\mathrm{d}u/\mathrm{d}y = 0$ or zero shear stress. For all deeper cavities the shear stress will take on negative values corresponding to reversed flow in the cavities.

The distribution of shear stress along the boundary for $\alpha = 65.12°$ is shown in figure 5(*a*). The shear stress is approximately equal to its undisturbed value $\tau_w = \tau^\infty$ just upstream of the cavity, rises very rapidly to become singular as it rounds the corner, and then drops quickly to reach zero at the centre of the cavity. A few points are worth noting. First, with respect to the discontinuous slope of the curve, we emphasize that this is merely to show the location of points where f is calculated. The Lagrangian interpolation used in the solution yields a smooth curve through these points. The singular behaviour of the shear stress at the corner is well known, as discussed by Dean & Montagnon (1949).

For convective-transport processes at high Prandtl numbers, the local mass-transfer rate is proportional to the shear stress (see e.g. Lighthill 1950 or Acrivos 1960). Thus

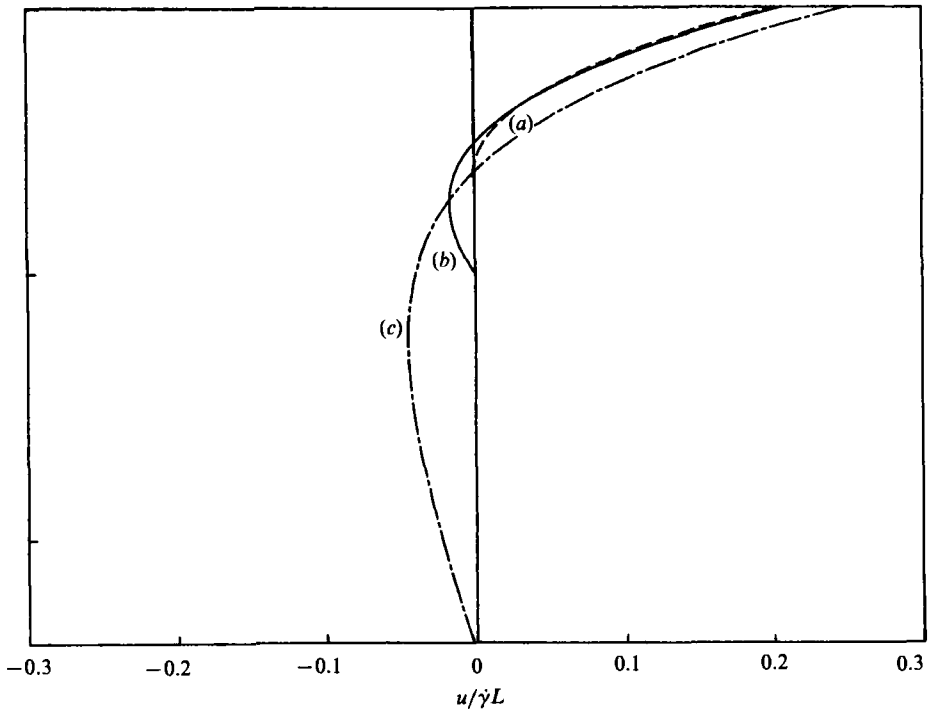

FIGURE 4. Velocity profiles for cavities in figure 3. Reference velocity is $\dot{\gamma}L$ where $2L$ is the width of cavity. Vertical scale for each curve extends from bottom of cavity to plane surface. (*a*) ----, $\alpha = 65.12°$; (*b*) ——, 90°; (*c*) ———, 135°.

the very low value of the shear stress across the bottom of the cavity implies slow mass transfer in this area. At the other extreme, transfer rates will be extremely high at the outer edge, resulting in rapid rounding of the corner if the surface is soluble.

When a cavity in a plane boundary is deeper than $\alpha = 65.12°$, a large recirculating eddy forms in the cavity. This is shown in figure 3(*b*) for a cavity $\alpha = 90°$. Two features are of interest. First, we see that the separation point is near, but not exactly at, the corner. This was previously noted by O'Neill (1977) and Wakiya (1975). The separation point for this case is at y approximately equal to -0.050. A second interesting feature of this pattern is that the separating streamline penetrates to a lesser degree than in the previous case. Thus we may conclude that the shallower cavity $\alpha = 65.12°$ in a certain sense represents the maximum disturbance to the outer flow. In comparing the two streamline patterns it is interesting to see how a relatively small increase in depth has resulted in an eddy which fills the entire cavity.

The velocity profile and shear stress for the 90° cavity are shown in figures 4(*b*) and 5(*b*) respectively. The velocity profile shows that the velocity in the eddy is quite small compared with the outer flow. This is reaffirmed in the shear-stress pattern, which shows a small nearly uniform negative shear stress over the entire cavity wall. The small value of the shear stress implies a small convective-transport rate at the cavity surface. Furthermore, the presence of the recirculating eddy prevents the passage of fresh fluid over the cavity wall. This can lead to an elevated concentration in the cavity, further decreasing the transfer rate. The inability of a shear flow to flush out deep cavities is a major problem in the cleansing of rough surfaces.

An extreme example of a circular cavity is shown in figure 3(*c*) for $\alpha = 135°$. Once

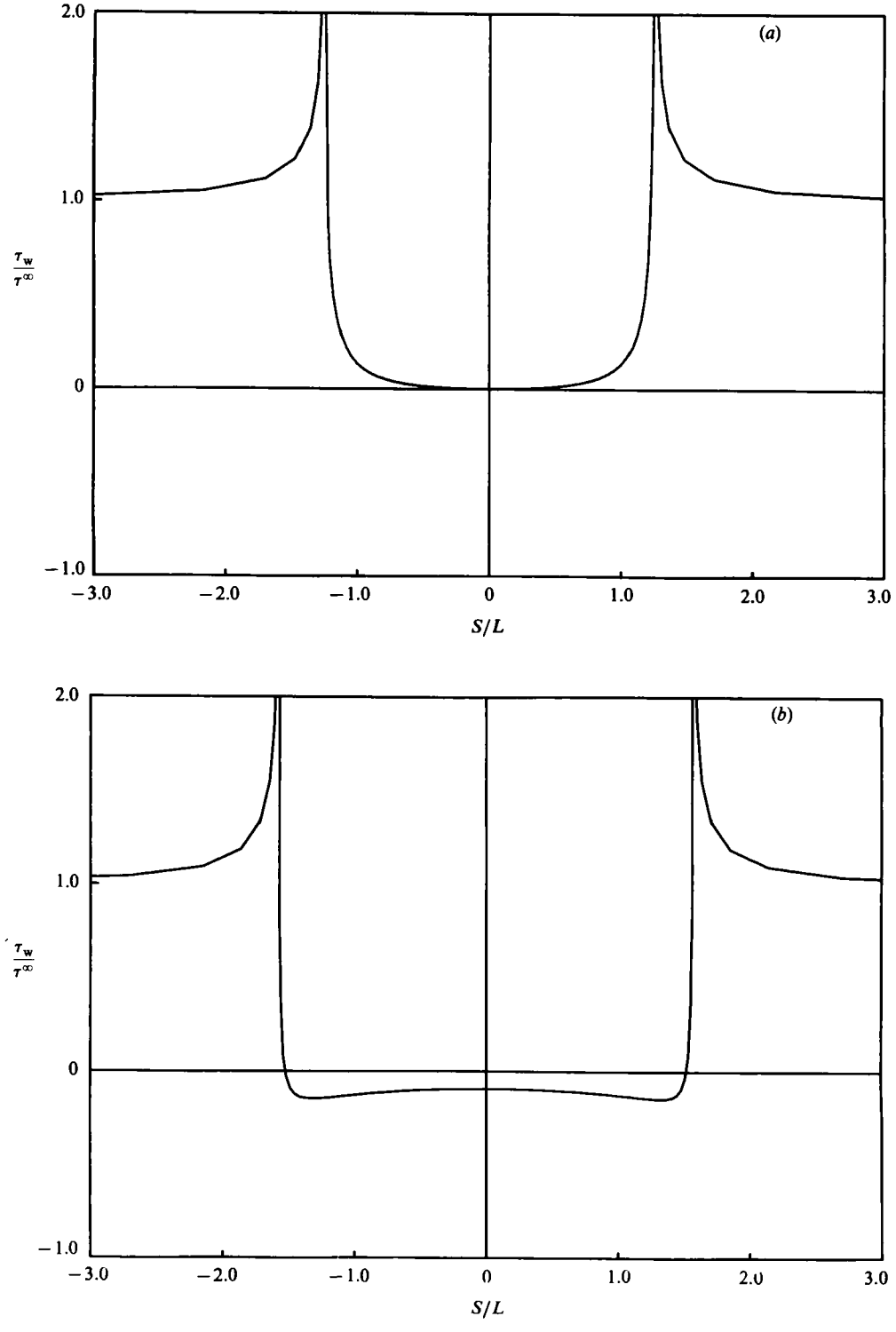

FIGURE 5(*a*, *b*). For description see facing page.

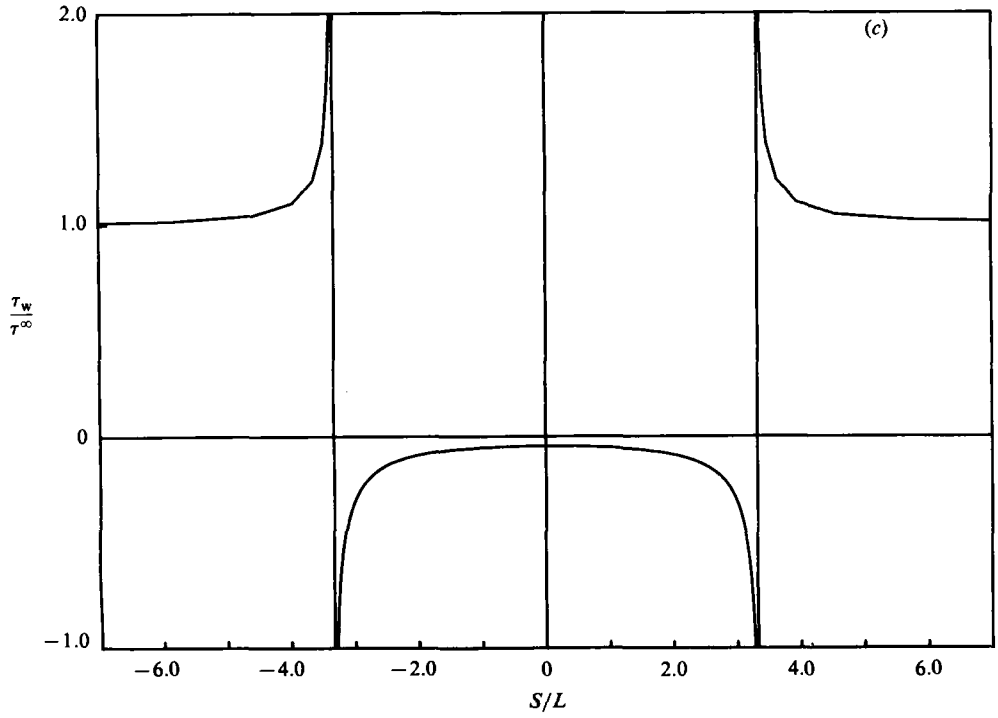

FIGURE 5. Shear stress as a function of position along wall for three cavities in figure 3. Undisturbed shear stress $\tau_w = \tau^\infty$. (*a*) $\alpha = 65.12°$, (*b*) 90°, (*c*) 135°.

again, we see that, as the cavity deepens, the disturbance of the outer flow lessens, while the attachment point approaches the corner. O'Neill (1977) has shown that, in the limit as $\alpha \to 180°$, the separation point reaches the corner and the separation streamline coincides with the plane. The velocity profile for the 135° cavity is similar to that for the 90° cavity except that the centre of the eddy is relatively higher in the cavity. The cavity velocities normalized with the width of the mouth are of the same order.

The shear stress for the 135° cavity shows interesting behaviour. Rather than a nearly uniform stress as in the 90° cavity, we see a large negative value near the top of the cavity. Contrary to the appearance of the figure, the negative shear stress is not singular but reaches a large finite value. In the limit as α approaches 180°, i.e. a slit separating two half-spaces, the negative value does become singular. Finally, we note that this large cavity presents an even greater problem for mass transfer than in the earlier cases, owing to the large volume of stagnant fluid and the small opening across which substances must diffuse.

5. Shear flow over rectangular cavities

In this section we continue our discussion of cavity flows by studying flow over rectangular cavities with width W and depth D. Certain of these flows have been studied previously using numerical methods cited in the introduction. As with the circular cavities our goal is to provide a comprehensive description of the flows with special relevance to transport processes. We start by considering a cavity with aspect ratio $W/D = 1$. The streamlines, velocity profile and shear stress are shown in

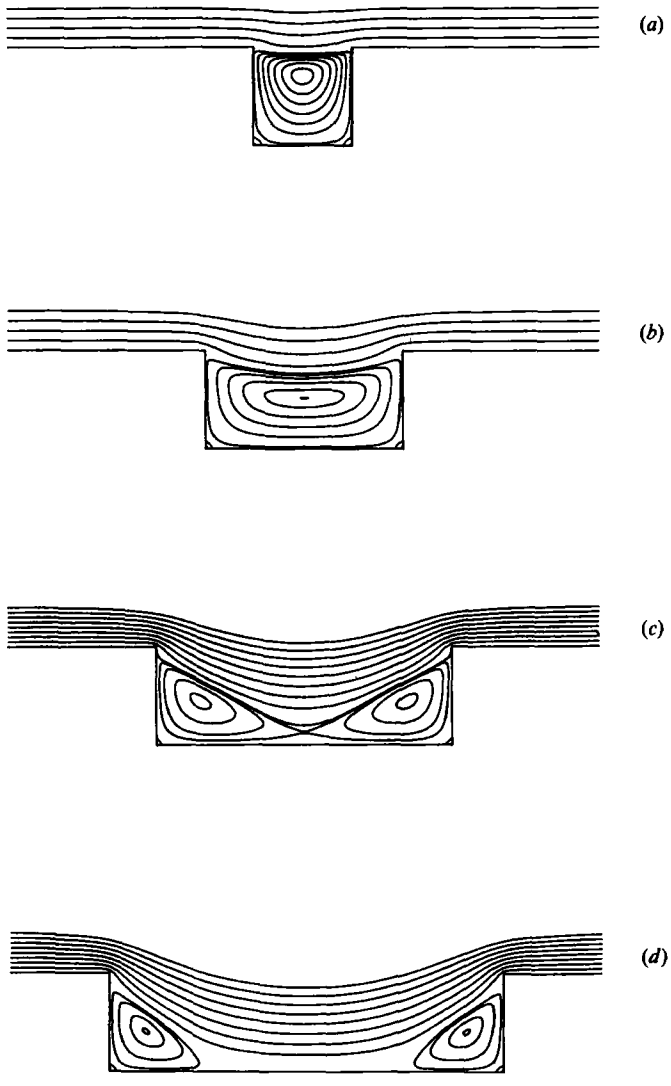

FIGURE 6. Streamline pattern for simple shear flow over rectangular cavities. Undisturbed flow is $u = \dot{\gamma}L$, $v = 0$. (*a*) aspect ratio 1:1, (*b*) 2:1, (*c*) 3:1, (*d*) 4:1.

figures 6(*a*), 7(*a*) and 8(*a*) respectively. In two major respects the flow is similar to that of the circular cavities: there is a single large eddy occupying the cavity, and the flow separates close to, but not at, the edge. One feature which is distinctly different is the presence of a sequence of eddies in the corners of the square, of which only the first can be seen in this figure. Moffat (1964) has described these eddies, showing that an infinite sequence exists obeying a simple similarity law.

In our calculations we have resolved only the first in the sequence of corner eddies; however, it is possible to use the boundary-integral method to resolve any number of eddies in the sequence. The procedure is to calculate the velocity at points along an arc or other curve enclosing the corner. This small sub-domain is then treated as a driven-cavity problem. Since the domain is smaller, finer resolution may be achieved. The process may be repeated as many times as required with ever smaller

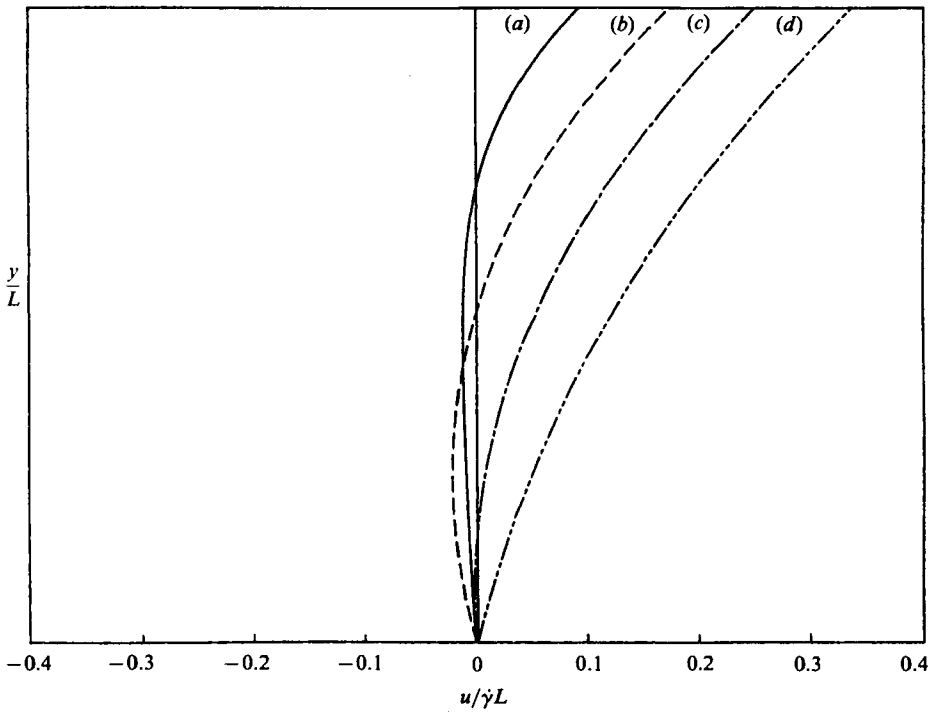

FIGURE 7. Velocity profiles for cavities in figure 6. Reference velocity is $\dot{\gamma}L$, where L is the depth of the cavity. (*a*) ——, aspect ratio 1:1; (*b*) – – –, 2:1; (*c*) ——–, 3:1; (*d*) ——–——, 4:1.

domains to resolve the desired detail. This is essentially analogous to the procedure used by Pan & Acrivos (1967) for their finite-difference calculations. One nice feature of the method is that the matrices A_{ij} and B_{ij} do not need to be recalculated, since each sub-domain is geometrically similar to the preceding one.

On examining the shear stress for the rectangular cavity, we see a pattern which is similar to that of the circular cavities. The principal features are the rapid increase leading to the singular value at the corner and the negative shear stress in the separated region of the cavity. The shear stress in the corners is zero, and τ_w is very small along the entire bottom of the cavity. The velocity profile is quite similar to those of the circular cavities. The relatively smaller magnitude of the velocity is due to the choice of the height as the reference length. This is appropriate for the cavities shown in figure 6, since width is varying.

Turning to our second rectangular cavity, with $W/D = 2$, we see that the large central eddy has been stretched to fill the cavity, leaving elongated streamlines in the centre. In other ways the flow is similar to that in the 1:1 cavity with the sequence of eddies in the corners. The velocity profile, figure 7(*b*), shows a stronger flow in the cavity with the centre of the eddy somewhat lower in the cavity. This increased velocity is to be expected since the cavity has a broader mouth across which the outer-driving flow may act. The shear stress, figure 8(*b*), confirms the stronger flow with a large negative value over the bottom of the cavity. In other respects the shear stress is nearly identical with that of the 1:1 cavity.

For a still wider cavity, $W/D = 3$, there is a dramatic change in the streamline pattern as shown in figure 6(*c*). First, we notice that the outer flow penetrates to a

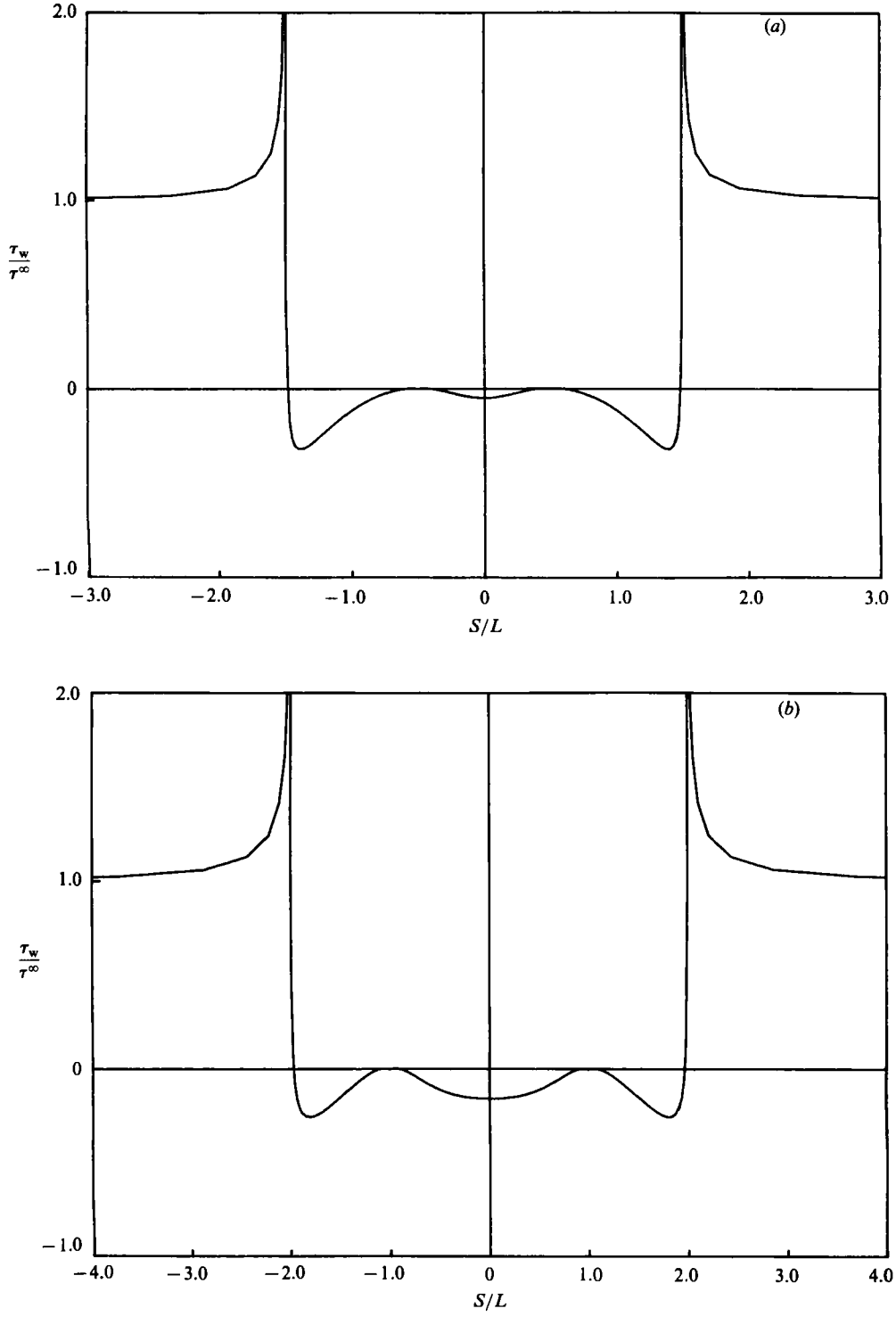

FIGURE 8(*a*, *b*). For description see facing page.

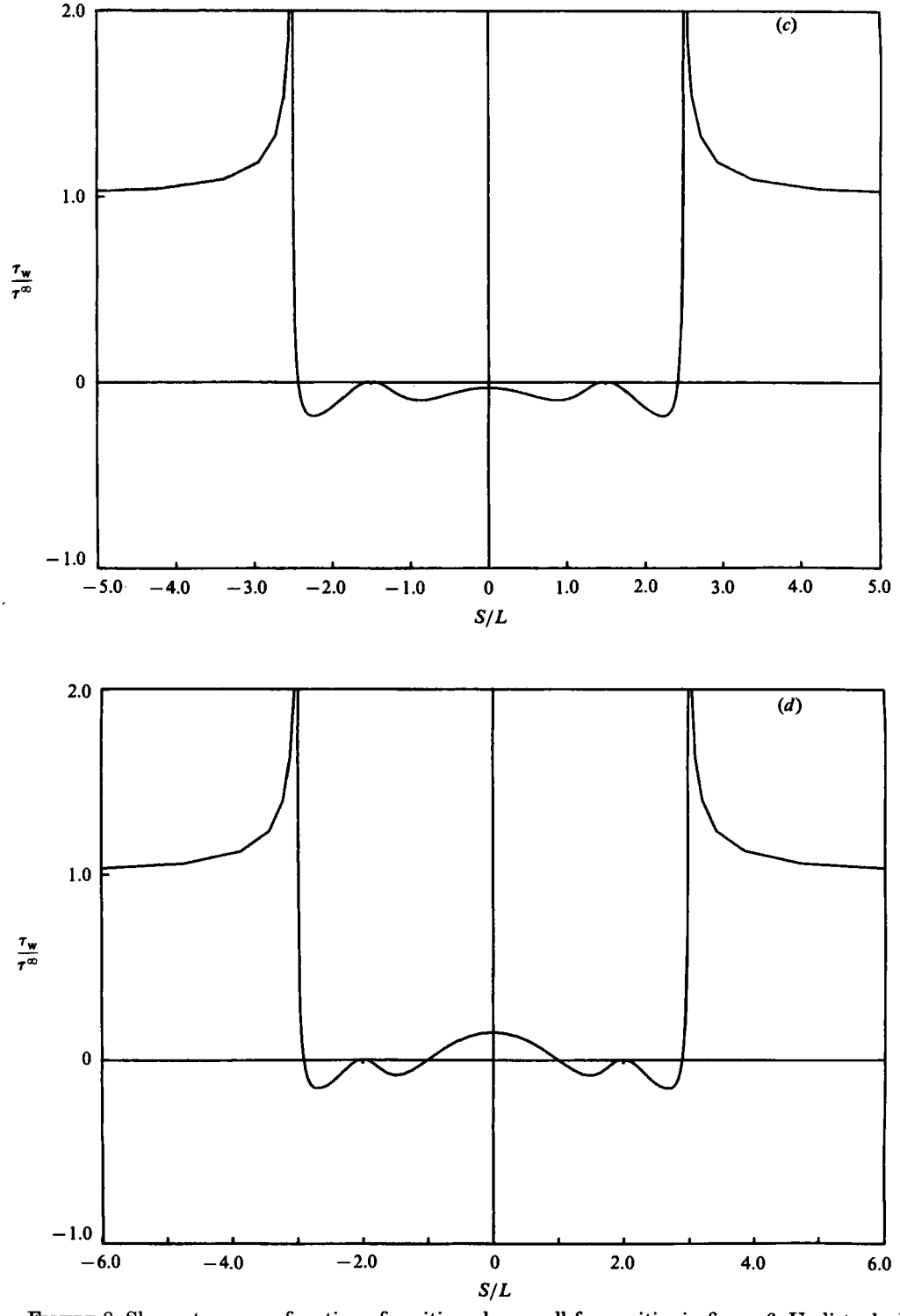

FIGURE 8. Shear stress as a function of position along wall for cavities in figure 6. Undisturbed shear stress $\tau_w = \tau^\infty$. (*a*) aspect ratio 1:1, (*b*) 2:1, (*c*) 3:1, (*d*) 4:1.

substantially greater depth. Further, the bulk of the recirculating region is now occupied by two eddies enclosed by a double-lobed separating streamline with an oblique stagnation point in the fluid away from the boundary. The sequence of corner eddies appears as before.

The deeper penetration of the outer flow is seen clearly in the velocity profile, figure 7(*c*). We see only a weak, almost imperceptible, reversed flow across the centre of the cavity. In the bulk of the cavity the flow moves forward with greater speed than in the other examples. The shear stress, figure 8(*c*), shows an unusual pattern reflecting the complicated flow in the cavity. Starting from its singular value at the corner, τ_w drops rapidly to zero and remains negative over the entire sidewall before rising to zero near the corner. It remains negative over the bottom wall, but rises almost to zero at the centre. The shear stress provides a clear indication of the weakness of the flow along the bottom wall.

The widest cavity considered in our calculations is shown in figure 6(*d*), with an aspect ratio of 4:1. In this case the outer flow has penetrated to the bottom of the cavity leaving a pair of isolated eddies in the corners. It is interesting that such a minor increase in the width has resulted in such a large portion of the cavity being swept by the outer flow. The strong influence of the outer flow in the cavity is also seen in the velocity profile, figure 7(*d*), which shows a nearly linear profile similar to that of the undisturbed flow. As might be expected, the shear stress for this flow is similar to the 3:1 cavity except that τ_w at the centre has risen above zero, reflecting the penetration of the outer flow. The overall picture of the flow for the 4:1 cavity is characteristic of all wide cavities. As the width is further increased the shear stress will approach its undisturbed value all along the base of the cavity. The corner eddies will maintain approximately the same size relative to the height and are independent of the width for wide cavities. The shear stress in the corner remains virtually unchanged for all wide cavities.

We have seen how the flow pattern changes as we proceed from a square cavity to greater widths; now it is appropriate to examine the behaviour as we approach greater depths. The streamline patterns for two cavities with aspect ratio 1:2 and 1:4 are shown in figure 9. For the 1:2 aspect ratio, a second compressed eddy has formed at the bottom of the cavity. For the deeper cavity three eddies have formed, with the upper two showing quite similar shapes. The aspect ratio of each of these eddies is approximately 1.40, which is nearly identical to the values reported by Pan & Acrivos (1967) and Moffat (1964). With the present results, we are able to verify that the simpler systems studied by these authors are legitimate models for flow over deep cavities.

The shear-stress distributions for the deep cavities are shown in figure 10. The shear stress around the corner and near the top of the sidewalls is similar to that observed for the shallower cavities. Deeper in the cavity the shear stress is negligible, reflecting the extremely weak flow at these depths.

A better view of the flow deep in the cavities is shown in the velocity profiles in figure 11. For clarity we have used a different velocity scale at different depths. The dashed lines correspond to the depths at which the separating streamline crosses the centre. The weakness of the flows is seen by the fact that maximum velocity in the last eddy for the 1:2 cavity is of order 10^{-4} times the reference velocity $(\tau^{\infty}/\mu)L$, where L is the cavity width. For the deeper cavity, the maximum is $10^{-7}(\tau^{\infty}/\mu)L$. These minute velocities are responsible for the difficulty in observing experimentally even the second in the sequence of eddies in deep cavities. Finally, we note that the similarity between the eddies in the 1:4 cavity is also reflected in the velocity profiles.

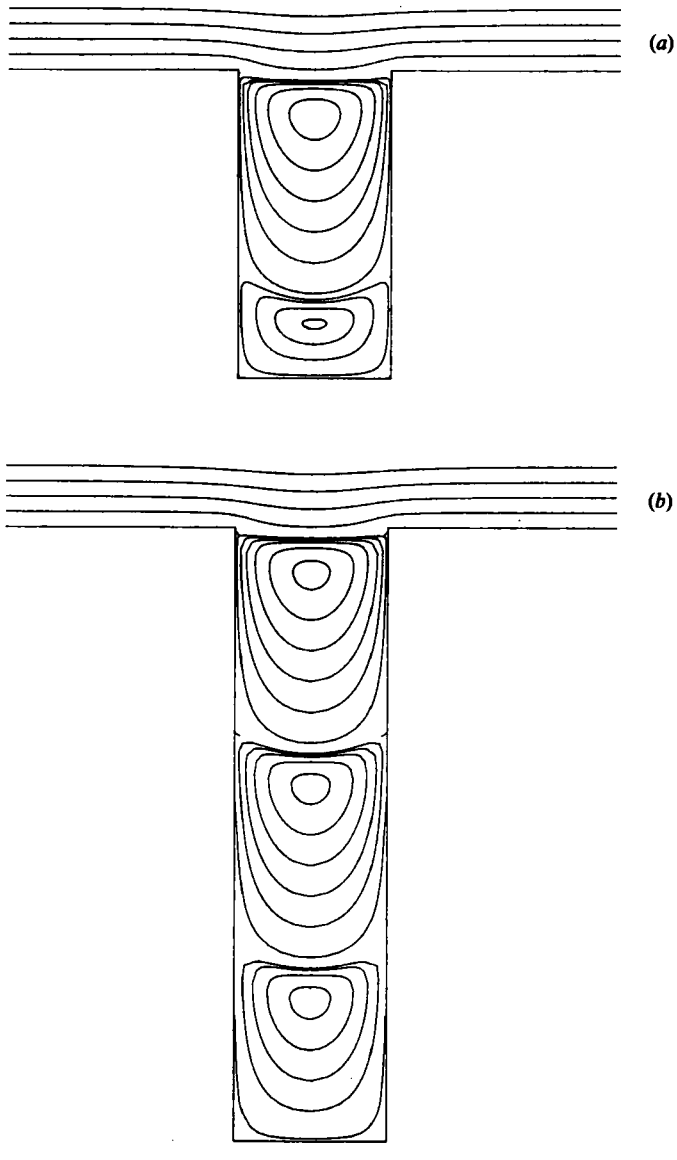

FIGURE 9. Streamline patterns for deep rectangular cavities. Undisturbed flow is $u = \gamma L$, $v = 0$. (*a*) aspect ratio 1:2, (*b*) 1:4.

With the exception of the sign reversal, the three profiles in figure 11 (*b*) are almost identical.

Reviewing the flow patterns we have observed above, we may draw a few qualitative conclusions about convective-transport processes in flow over rectangular cavities. First, and most importantly, we conclude that a simple transverse shear flow is very ineffective in flushing out a deep cavity. If the flow is to penetrate to the bottom of the cavity, the width must be 3–4 times the depth. Even in this case, the sidewalls and corners of the cavity will be in a stagnant recirculating region. In all cases the singular shear stress at the corner will lead to high transfer rates with rapid eroding of the sharp edge.

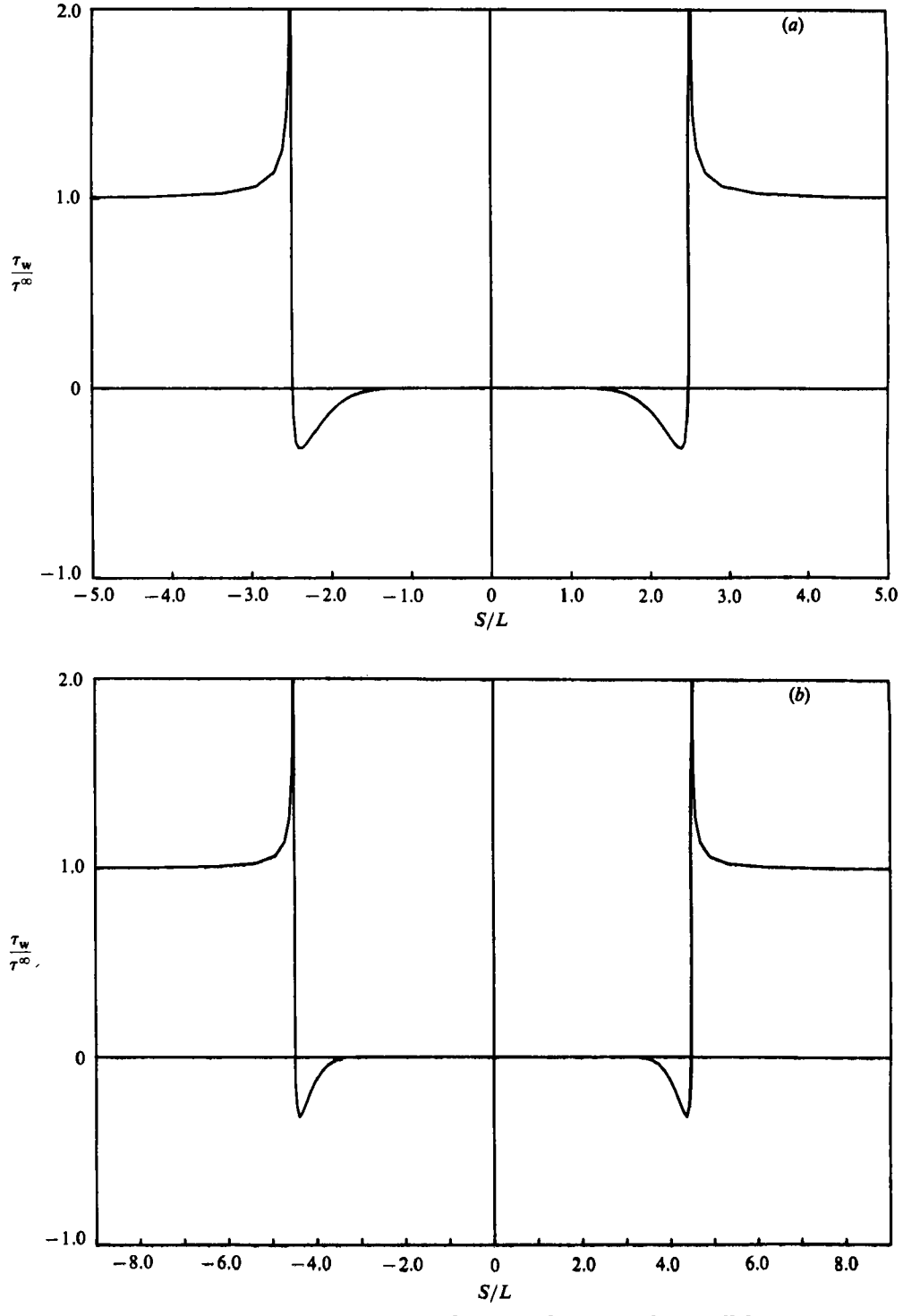

FIGURE 10. Shear stress as a function of position along wall for cavities in figure 9. (*a*) aspect ratio 1:2, (*b*) 1:4.

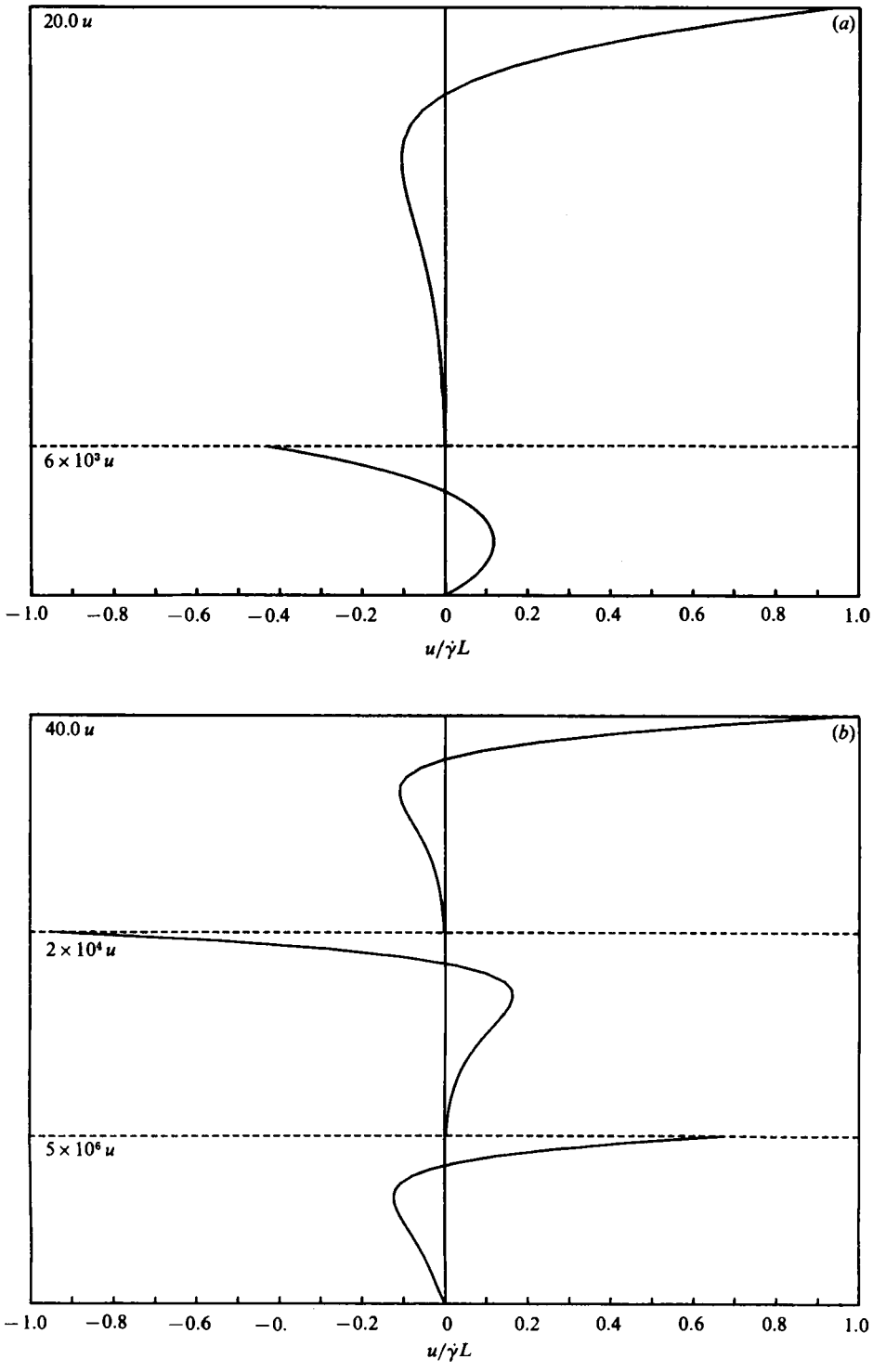

FIGURE 11. Velocity profiles for deep cavities in figure 9. Reference velocity is $\dot{\gamma}L$, where L is width of cavity. Dotted lines are depths of dividing streamlines. (*a*) aspect ratio 1:2, (*b*) 1:4.

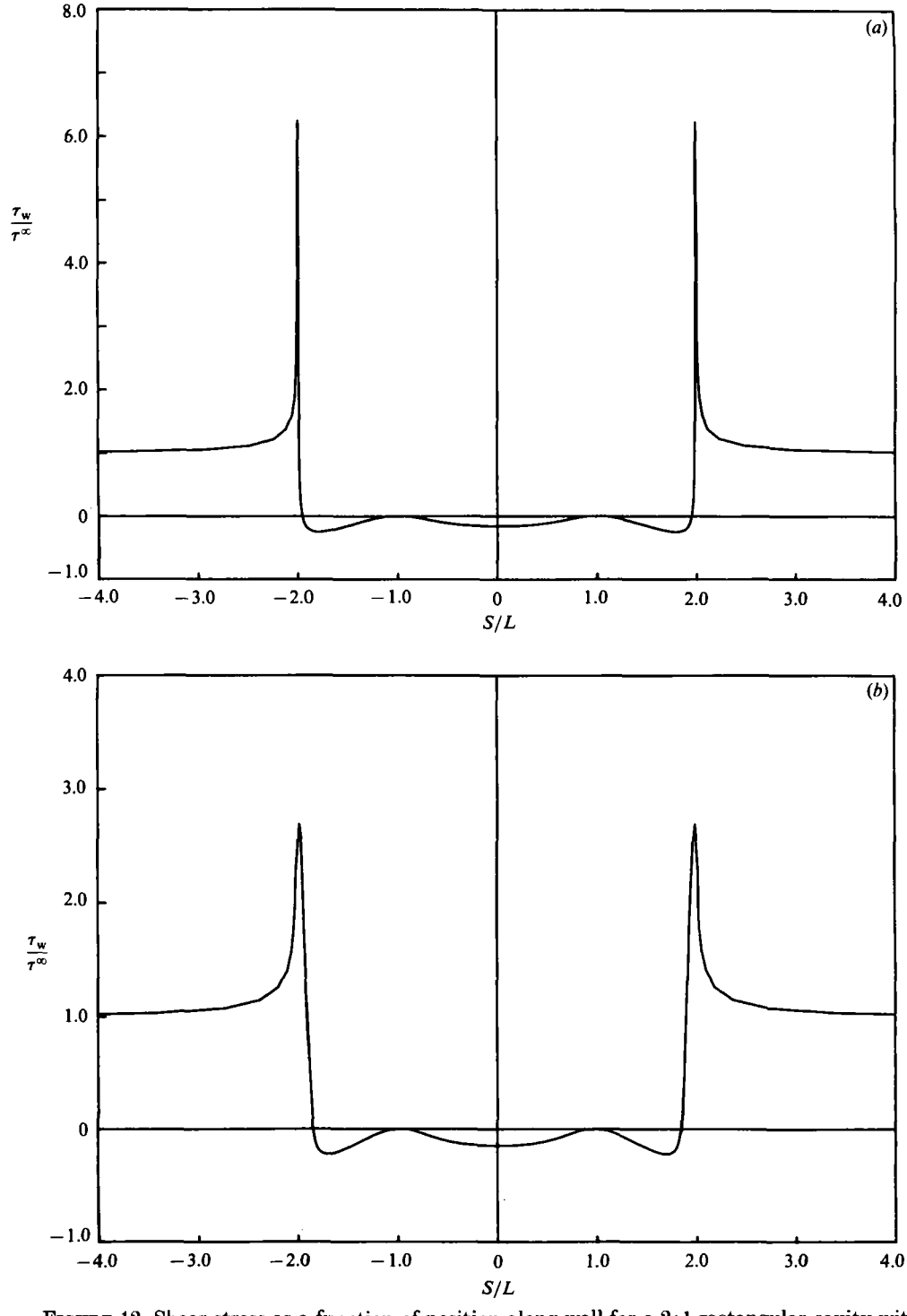

FIGURE 12. Shear stress as a function of position along wall for a 2:1 rectangular cavity with rounded corners. (*a*) corner radius, $A = 0.01D$, (*b*) $0.10D$.

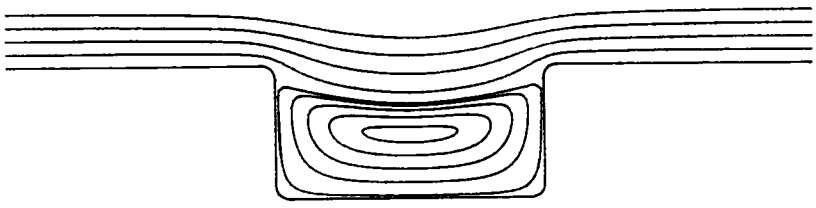

FIGURE 13. Streamline pattern for 2:1 rectangular cavity with $0.10D$-radius rounded corners.

5.1. *The effect of rounded corners*

One of the features of flow over rectangular cavities which has raised some questions in the literature is the effect of rounded corners on the motion. Clearly, if the corner is rounded, the shear stress becomes bounded, but it is not clear how strongly this will affect the overall motion. In the present work we consider a typical rectangular cavity with 2:1 aspect ratio and evaluate the effect of rounding the corners of the solid boundary. We start with a fairly sharp corner with radius equal to $0.01D$, where D is the depth of the cavity. For this case the streamlines are indistinguishable from the pattern for a sharp corner as shown earlier in figure 6(*b*). It is only in the shear stress, figure 12(*a*), that we see a measurable difference. For the rounded corner the shear stress develops a sharp peak, but the peak is finite with a value of 6.22 ± 0.005. In other respects, the stress is the same as in the sharp-corner cavity.

To assess the effect of a greater rounding of the edge, we next consider a cavity with corner radius $0.1D$. The streamlines for this case are shown in figure 13. The pattern resembles the sharp-corner case, but the separation point is lower on the sidewall, and the outer flow penetrates slightly deeper into the cavity. The shear stress for the $0.1D$ cavity is shown in figure 12(*b*). The effect of the rounding is apparent as the maximum shear stress has fallen to 2.70 ± 0.005. The stress distribution away from the corner is similar to the other cavities, although the magnitude of the stress at the centre is slightly less, -0.148 compared with -0.160 for the sharp corner. This is a consequence of the deeper penetration of the flow into the cavity.

6. Shear flow over circular ridges

Having completed our discussion of flow over cavities, we turn our attention to the problem of flow over two-dimensional ridges, starting in this section with circular ridges. This has been the subject of a number of studies, including the analytical work of O'Neill (1977) and Wakiya (1975, 1978) mentioned earlier. In addition, Davis & O'Neill (1977) and Jeffrey & Sherwood (1980) have examined these solutions as model problems for separated flow.

In this section, we will provide a brief discussion of these flows, giving special consideration to the effect on convective transport. We start with the flow over a small ridge with $\alpha = 34°$, where α is as defined previously except that the arc is now above the plane. This angle corresponds to the maximum angle for which the flow does not separate in the corners, (Moffat 1964). In the streamline pattern, figure 14(*a*), we see negligible disturbance of the flow with only a smooth bending of the streamlines around the obstacle. From this picture of the flow field we might expect only a mild disturbance of the shear stress on the wall. Figure 15(*a*) gives quite a different view, as τ_w is markedly changed from its uniform undisturbed value. The shear stress drops rapidly to zero in the corner and then rises to nearly twice τ^∞ at

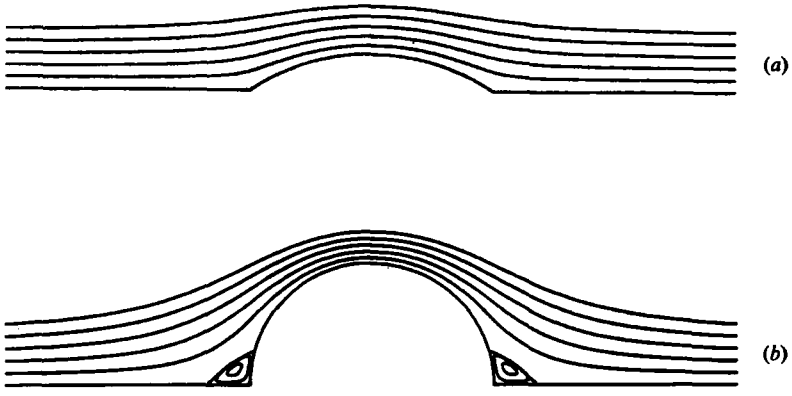

FIGURE 14. Streamline pattern for simple shear flow over circular crests. (*a*) $\alpha = 34°$, (*b*) 90°.

the crest. Clearly, the smooth streamlines give a deceptive indication of the strength of the flow disturbance.

From the viewpoint of convective-transport processes, the stress distribution shown in figure 15(*a*) has important consequences. First, it indicates that there will be very poor mass transfer into or out of the corners. This presents a serious problem in those industrial applications where it is essential to provide a uniform coating over a ridge and the adjoining surface of the plane substrate. Conversely, there will be high mass transfer at the crest, owing to the large shear stress at that point. This is consistent with the rapid smoothing which occurs on an eroding or dissolving surface. If a surface is being deposited by convective mass transfer, the rate of deposition will be largest at the crest, leading to a rapid steepening of the ridge. Thus, small disturbances on a surface will rapidly grow into sharp well-defined ridges.

We study the change in the flow for steeper obstacles by considering a ridge with $\alpha = 90°$ in figure 14(*b*). Now the disturbance to the flow is more pronounced, with corner eddies at the base of the obstacle and a definite pinching of the streamlines over the crest. The shear-stress plot in figure 15(*b*) confirms this view. The acceleration of the fluid over the crest has resulted in a stress approximately 3 times the undisturbed value τ^{∞}, while the weak recirculating flow in the eddies is shown by the small negative values of τ_w in the corners. It is interesting to note how the smooth rounded obstacle has produced eddies much smaller than its vertical dimension. This contrasts with the results for cavities and for sharp crests, which we examine in the following section.

For convective transport the shear stress for the 90° ridge amplifies the mechanisms described above. The rate of deposition onto the crest will be still greater, while the eddies effectively shield the base with a layer of stagnant fluid. Thus we see that the hydrodynamic effects on mass transfer will lead to the formation of sharp well-defined ridges, or, analogously, long thin filaments or dendrites.

The two ridges discussed above show the essential features of flow over cylindrical obstacles. For greater values of α the corner eddies increase in size and the stress on the crest becomes even greater. Streamlines for large values of α may be found in the references cited earlier.

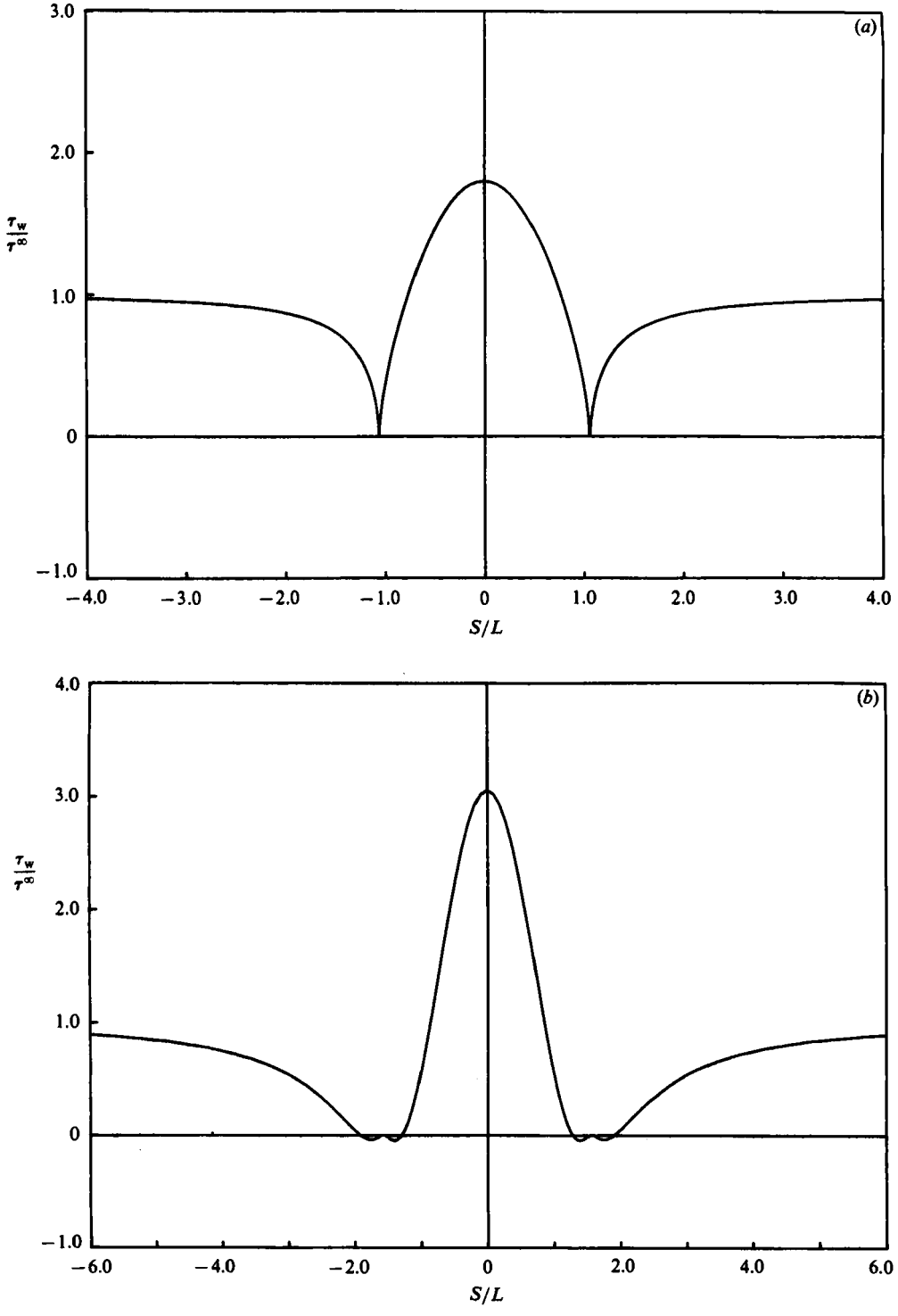

FIGURE 15. Shear stress as a function of position along wall for ridges shown in figure 14. (*a*) $\alpha = 34°$, (*b*) 90°.

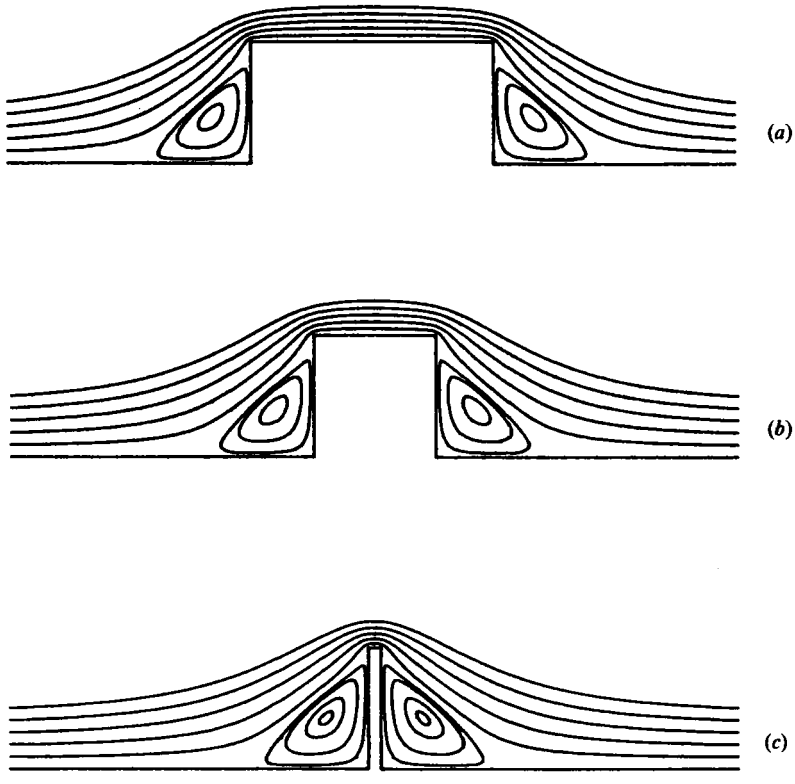

FIGURE 16. Streamline patterns for simple shear flow over rectangular crests. (*a*) aspect ratio 2:1, (*b*) 1:1, (*c*) 1:10.

7. Shear flow over rectangular ridges

Our final series of calculations involves flow over rectangular obstacles. We start by considering a rectangle with aspect ratio 2:1 as shown in figure 16(*a*). This has the same width-to-height ratio as the 90° circular crest studied in the last section. The streamline pattern shows major changes in the flow owing to the sharp profile of the obstacle. We note that the eddies are much larger and almost equal to the height of the ridge. This eddy configuration is characteristic of all rectangular ridges and is quite insensitive to aspect ratio.

The shear stress for the 2:1 ridge is shown in figure 17(*a*). As before, the shear stress is singular as the fluid rounds the corner of the solid boundary. One interesting feature is that the shear stress in the centre is lower than for the 90° crest. This is owing to the broad flat top of the ridge which provides greater surface area to decelerate the flow. In other respects the shear stress is similar to the distribution for the circular crest.

The 2:1 rectangular obstacle is characteristic of all wide, flat ridges. As the width is further increased, the streamlines remain virtually unchanged. The shear stress upstream and downstream is also insensitive to the width. The only noticeable change is that the stress at the centre will gradually fall to the undisturbed value τ^{∞} as the width increases.

For narrower ridges the flow pattern changes only gradually until the aspect ratio

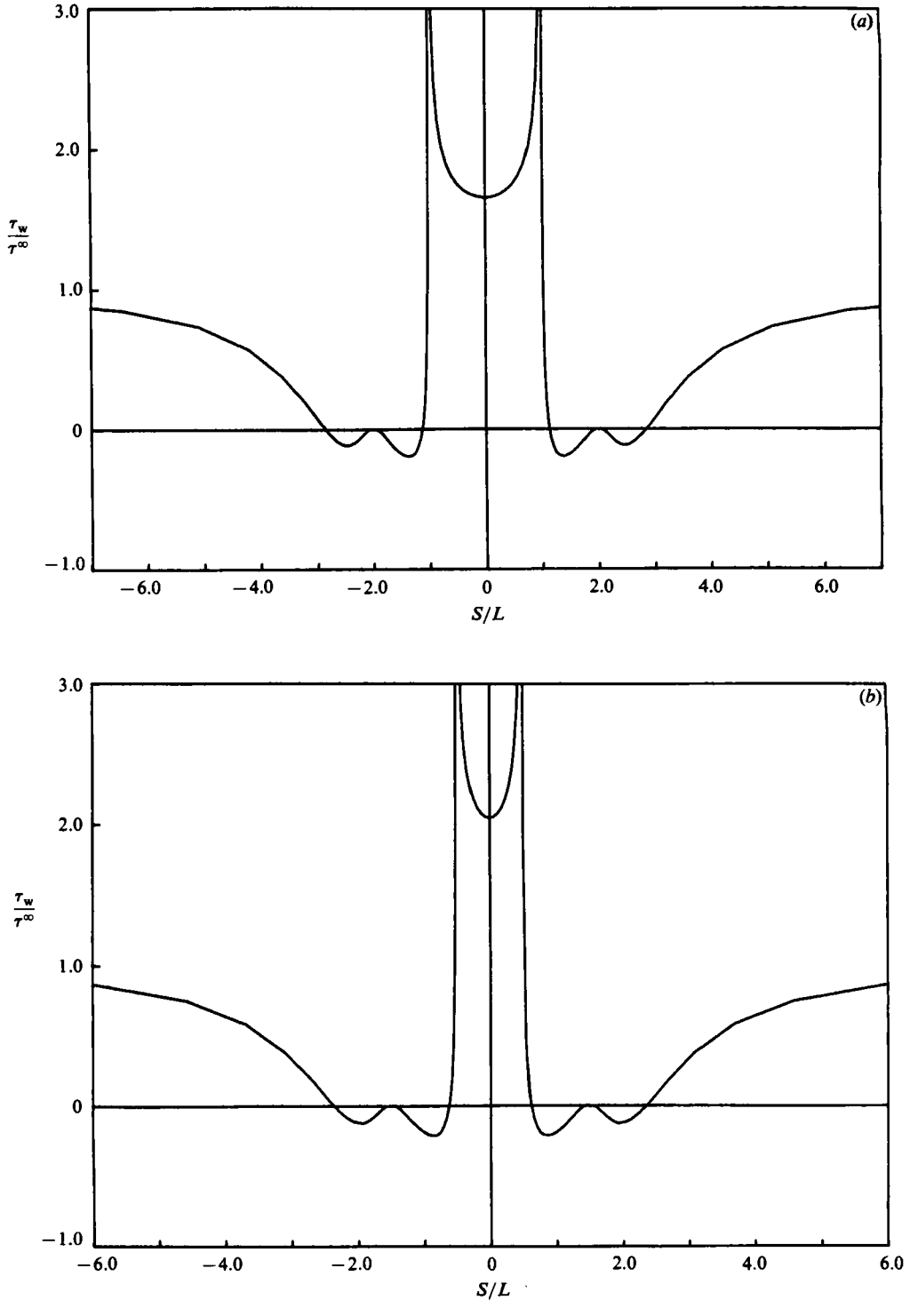

FIGURE 17 (*a*, *b*). For description see next page.

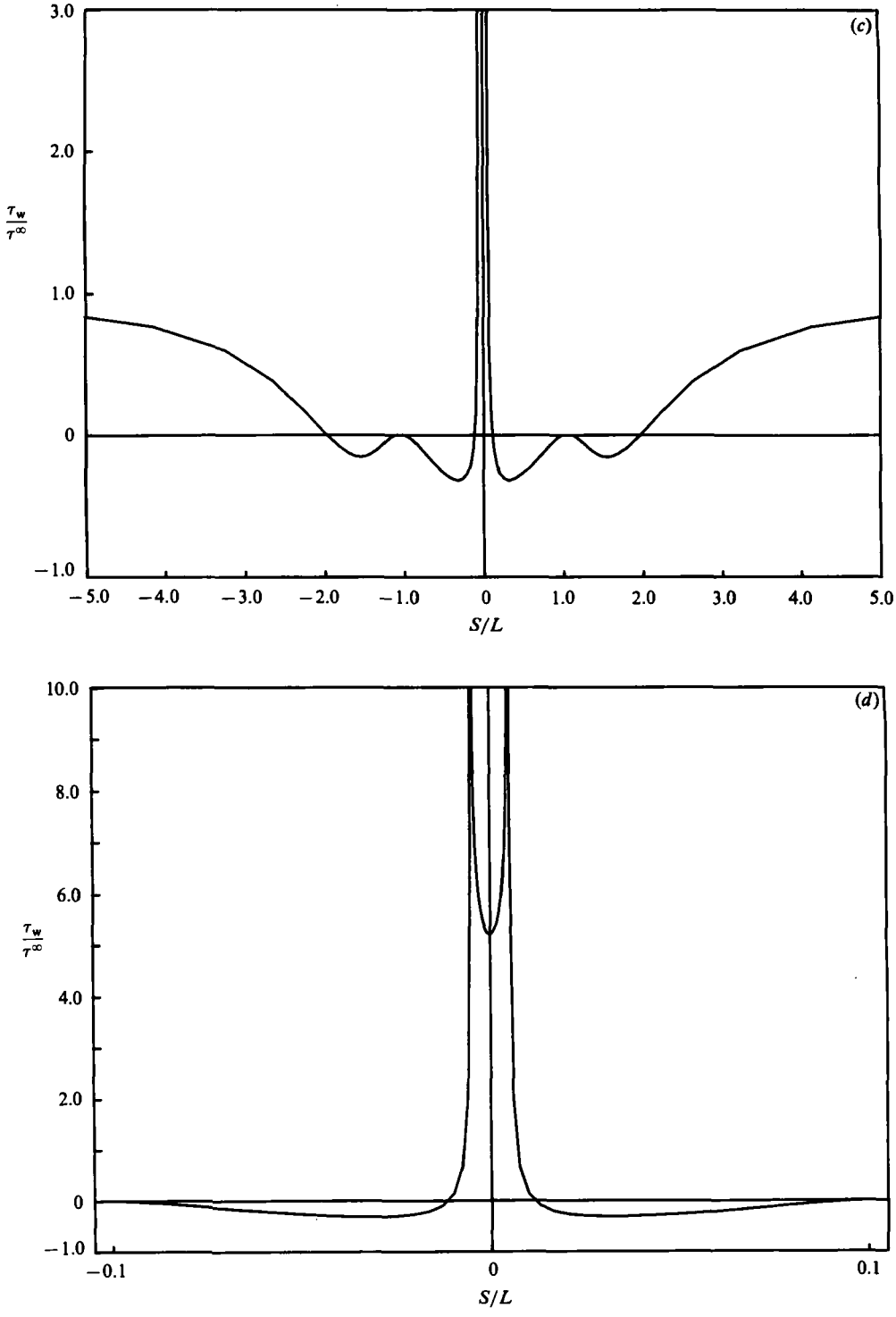

FIGURE 17. Shear stress as a function of position along wall for ridges in figure 16. (*a*) aspect ratio 2:1, (*b*) 1:1, (*c*) 1:10, (*d*) expanded version of (*c*) showing only top and sides of crest.

becomes quite small. Figure 16(*b*) shows a 1:1 rectangular ridge with streamline pattern almost identical to the 2:1 case. Similarly, the shear stress in figure 17(*b*) closely resembles the previous case. The major difference in the 1:1 plot is that a greater portion of the top surface is affected by the large shear stress at the corners.

To see an appreciable difference in the flow behaviour we examine a thin obstacle with aspect ratio 1:10. Once again, the pattern of eddies, figure 16(*c*), is the same, but the long straight streamlines over the crest have been eliminated owing to the narrowness of the obstacle. The narrow plateau experiences an extremely large shear stress as the two corners are so close as to dominate the stress distribution on the top, figure 17(*c*). A clearer view of this region is shown in figure 17(*d*), where τ_w has been replotted on a different scale, showing only the top and sides of the ridge. We see that the minimum stress at the centre is now 5 times the undisturbed value. It is interesting to note that the basic shape of the distribution is similar to that observed for the wider crests.

Convective transport for flow over rectangular ridges shares many of the features of the earlier flows we have studied. As with the sharp-edge cavities, we infer that the corners of a soluble ridge will rapidly be dulled owing to the high transfer rates. For surfaces of deposition, the situation is similar to that for circular crests with the eddies shielding the base, while the high shear stress encourages the growth of the crest. A slight difference is that the stress distribution on the rectangular ridges would tend to favour the formation of twin peaks near the edges, with a depression in between. This could eventually lead to the development of two separate peaks which would be susceptible to further splitting.

REFERENCES

Acrivos, A. 1960 Solution of the laminar boundary layer energy equation at high Prandtl numbers. *Phys. Fluids* **3**, 657–658.

Carnahan, B., Luther, H. A. & Wilkes, J. O. 1969 *Applied Numerical Methods*. Wiley.

Davis, A. M. J. & O'Neill, M. E. 1977 Separation in a slow linear shear flow past a cylinder and a plane. *J. Fluid Mech.* **81**, 551–564.

Dean, W. R. & Montagnon, P. E. 1949 On the steady motion of a viscous liquid in a corner. *Proc. Camb. Phil. Soc.* **45**, 389–394.

Happel, J. & Brenner, H. 1973 *Low Reynolds Number Hydrodynamics*, 2nd Edn. Noordhoff.

Hasimoto, H. & Sano, O. 1980 Stokeslets and eddies in creeping flow. *Ann. Rev. Fluid Mech.* **12**, 335–363.

Higdon, J. J. L. 1979*a* The generation of feeding currents by flagellar motions. *J. Fluid Mech.* **94**, 305–330.

Higdon, J. J. L. 1979*b* The hydrodynamics of flagellar propulsion: helical waves. *J. Fluid Mech.* **94**, 331–351.

Hinch, E. J. 1972 Note on the symmetries of certain matersial tensors for a particle in Stokes flow. *J. Fluid Mech.* **54**, 423–425.

Jackson, N. & Finlayson, B. A. 1982 Calculation of the hole pressure. I. Newtonian fluids. *J. Non-Newtonian Fluid Mech.* **10**, 55–69.

Jeffrey, D. J. & Sherwood, J. D. 1980 Streamline patterns and eddies in low Reynolds number flow. *J. Fluid Mech.* **96**, 315–334.

Kim, M.-U. 1980 Slow viscous flow around a vertical fence on a plane. *J. Phys. Soc. Japan* **49**, 2387–2391.

Lee, S. H. & Leal, L. G. 1982 The motion of a sphere in the presence of a deformable interface. *J. Colloid Interface Sci.* **87**, 81–106.

Lighthill, M. J. 1950 Contributions to the theory of heat transfer through a laminar boundary layer. *Proc. R. Soc. Lond.* A **202**, 359–377.

LORENTZ, H. A. 1896 *Amsterdam, Zittingsverlag Akad.v. Wet.* **5**, 168.

MALKUS, D. S. 1976 In *Proceedings of the VII Intl Congr. on Rheology, Gothenberg, Sweden* (ed. C. Klason & J. Kubat), pp. 00–00.

MIKHLIN, S. G. 1957 *Integral Equations.* Macmillan.

MIR-MOHAMAD-SADEGH, S. & RAJAGOPAL, K. R. 1980 The flow of a non-Newtonian fluid past projections and depressions. *Trans. ASME* E: *J. Appl. Mech.* **47**, 485–488.

MOFFATT, H. K. 1964 Viscous and resistive eddies near a sharp corner. *J. Fluid Mech.* **18**, 1–18.

O'BRIEN, V. 1982 Viscous flow in an annulus with a sector cavity. *Trans. ASME* I: *J. Fluids Engng* **104**, 500–504.

O'BRIEN, V. 1983 Flow in pressure holes. *J. Non-Newtonian Fluid Mech.* **12**, 383–386.

O'NEILL, M. E. 1977 On the separation of a slow linear shear flow from a cylindrical ridge or trough in a plane. *Z. angew. Math. Phys.* **28**, 439–448.

PAN, F. & ACRIVOS, A. 1967 Steady flows in rectangular cavities. *J. Fluid Mech.* **28**, 643–655.

RALLISON, J. M. & ACRIVOS, A. 1978 A numerical study of the deformation and burst of a viscous drop in an extensional flow. *J. Fluid Mech.* **89**, 191–200.

SANDERS, J., O'BRIEN, V. & JOSEPH, D. D. 1980 Stokes flow in a driven sector by two different methods. *Trans. ASME* E: *J. Appl. Mech.* **47**, 482–484.

TAKEMATSU, M. 1966 Slow viscous flow past a cavity. *J. Phys. Soc. Japan* **21**, 1816–1821.

TROGDON, S. A. & JOSEPH, D. D. 1982 Matched eigenfunction expansions for slow flow over a slot. *J. Non-Newtonian Fluid Mech.* **10**, 185–213.

WAKIYA, S. 1975 Application of bipolar coordinates to the two dimensional creeping motion of a liquid. I. Flow over a projection or depression on a wall. *J. Phys. Soc. Japan* **39**, 1113–1120.

WAKIYA, S. 1978 Application of bipolar coordinates to the two dimensional creeping motion of a liquid. III. Separation in Stokes flow. *J. Phys. Soc. Japan* **45**, 1756–1763.

YOUNGREN, G. K. & ACRIVOS, A. 1975 Stokes flow past a particle of arbitrary shape: a numerical method of solution. *J. Fluid Mech.* **69**, 377–403.